

Really Cool Stars and the Star Formation History at the Galactic Center

R. D. Blum¹

Cerro Tololo Interamerican Observatory, Casilla 603, La Serena, Chile
rblum@ctio.noao.edu

Solange V. Ramírez¹

SIRTF Science Center, JPL/Caltech, Pasadena, CA 91125, USA
solange@astro.caltech.edu

K. Sellgren¹

Astronomy Department, The Ohio State University, 140 West 18th Ave, Columbus, OH
43210, USA
sellgren@astronomy.ohio-state.edu

K. Olsen

Cerro Tololo Interamerican Observatory, Casilla 603, La Serena, Chile
kolsen@noao.edu

ABSTRACT

We present $\lambda/\Delta\lambda = 550$ to 1200 near infrared H and K spectra for a magnitude limited sample of 79 asymptotic giant branch and cool supergiant stars in the central ≈ 5 pc (diameter) of the Galaxy. We use a set of similar spectra obtained for solar neighborhood stars with known T_{eff} and M_{bol} that is in the same range as the Galactic center (GC) sample to derive T_{eff} and M_{bol} for the GC sample. We then construct the Hertzsprung–Russell (HRD) diagram for the GC sample. Using an automated maximum likelihood routine, we derive a coarse star formation history of the GC. We find (1) roughly 75% of the stars formed in the central few pc are older than 5 Gyr; (2) the star formation rate (SFR) is variable over time, with a roughly 4 times higher star formation rate in the last

¹Visiting Astronomer, Cerro Tololo Interamerican Observatory, National Optical Astronomy Observatories, which is operated by Associated Universities for Research in Astronomy, Inc., under cooperative agreement with the National Science Foundation

100 Myr compared to the average SFR; (3) our model can only match dynamical limits on the total mass of stars formed by limiting the IMF to masses above $0.7 M_{\odot}$. This could be a signature of mass segregation or of the bias toward massive star formation from the unique star formation conditions in the GC; (4) blue supergiants account for 12 % of the total sample observed, and the ratio of red to blue supergiants is roughly 1.5; (5) models with isochrones with $[\text{Fe}/\text{H}] = 0.0$ over all ages fit the stars in our HRD better than models with lower $[\text{Fe}/\text{H}]$ in the oldest age bins, consistent with the finding of Ramirez et al. (2000) that stars with ages between 10 Myr and 1 Gyr have solar $[\text{Fe}/\text{H}]$.

Subject headings: Galaxy: center — stars: late-type — stars: AGB and post-AGB — supergiants

1. INTRODUCTION

The properties of the stellar population at the Galactic Center (GC) suggest that the nucleus is distinct from the other main structural components of the Galaxy (the Galactic disk, bulge, and Halo), though each of these components may contribute to the integrated population. We would like to distinguish between extensions of these populations and a unique GC population which has formed and evolved there. OH/IR stars distributed in an inner disk between ~ 1 and 100 pc (Lindqvist, Habing, & Winnberg 1992) show higher rotational velocities than expected for a “hot” bulge component, suggesting a disk like population. Near infrared surface brightness measurements indicate the bright nucleus joins the bulge discontinuously at a radius of about 150 pc; see the discussion given by Kent (1992) which relies in part on the $4 \mu\text{m}$ minor axis surface brightness profile presented by Little & Price (1985). Recent work on detailed abundance determinations in the central 60 pc (Carr et al. 2000; Ramírez et al. 2000) also reveal differences between the Galaxy’s nucleus and bulge components. Ramírez et al. (2000) find a narrow distribution in $[\text{Fe}/\text{H}]$ in the GC peaked around the solar value, while the bulge has a very broad distribution in $[\text{Fe}/\text{H}]$ with a mean less than the solar value (McWilliam & Rich 1994; Sadler, Rich, & Terndrup 1996).

Stars as young as $\lesssim 5$ Myr are now known to exist in the central pc. Very recent star formation was clearly established by Forrest et al. (1987) and Allen, Hyland, & Hillier (1990) with the discovery of a bright, evolved, and massive emission–line star (the “AF” star). Krabbe et al. (1991) further showed that a significant component of the strong recombination lines of H and He seen toward the GC arises in spatially compact sources, particularly the “IRS 16” cluster of massive stars (Najarro et al. 1994; Libonate et al. 1995; Blum et al. 1995a; Krabbe et al. 1995; Blum et al. 1995b; Tamblyn et al. 1996; Najarro et al. 1997).

Krabbe et al. (1995) have modeled the IRS 16 cluster as the evolved descendants of the most massive stars ($\sim 100 M_{\odot}$) belonging to a $\lesssim 7$ Myr old burst.

In their review of the global phenomena on-going in the GC region, Morris & Serabyn (1996) described the properties of the “central molecular zone,” or CMZ. The CMZ is a “disk” of enhanced molecular density about 200 pc in radius centered on the GC. The gas is confined to a region near the plane of the Galaxy, but with significant non-circular motions. The distribution and presence of molecular gas in the CMZ may in large part be due to the effects of the inner Galactic stellar bar (Liszt & Burton 1980; Mulder & Liem 1986; Binney et al. 1991; Blitz & Spergel 1991; Weiland et al. 1994; Dwek et al. 1995; Stanek et al. 1994). The material in the CMZ is fueling current star formation on this large scale at a rate of about $0.5 M_{\odot} \text{ yr}^{-1}$ (Güsten 1989), but it may also be the ultimate source of material which is processed into stars within a few pc of the GC (Morris & Serabyn 1996). If so, angular momentum losses must funnel the gas down to the circumnuclear disk (CND) at radii between ~ 2 and 8 pc (see the extensive reviews by Genzel, Hollenbach, & Townes 1994 and Morris & Serabyn 1996). This molecular structure is probably not a long-lived one, but rather periodically forms and supplies the GC with star forming material through instabilities which cause material to fall from its inner radius into the central pc (Sanders 1999); at present the CND may be accreting about $0.5 \times 10^{-2} M_{\odot} \text{ yr}^{-1}$ (Güsten et al. 1987; Jackson et al. 1993).

In this paper, we continue the exploration of the stellar content of the central few pc of the Milky Way begun by Blum, DePoy, & Sellgren (1996*a*, hereafter BDS96) and Blum, Sellgren, & DePoy (1996*b*, BSD96). Using J , H , and K photometry, BDS96 identified a bright component to the dereddened K -band luminosity function relative to the Galactic bulge population seen toward Baade’s Window (BW), which is predominantly old ($\gtrsim 10$ Gyr; Terndrup 1988; Lee 1992; Holtzman et al. 1993). Specifically, BDS96 compared K -band counts in the central few pc to those in BW presented by Tiede, Frogel, & Terndrup (1995). BSD96 presented a small sample of near infrared spectra which they used to begin a detailed investigation of the properties of the cool stellar population in the Galactic center (GC), including the ages of individual stars which trace multiple epochs of star formation there. This work, in turn, is built on earlier work, most notably that of Lebofsky, Rieke, & Tokunaga (1982*a*) who investigated recent star formation in the GC using the luminous and young M-type supergiants they identified there.

Our goal is to determine T_{eff} and M_{bol} for a magnitude limited sample of GC stars, using the two-dimensional classification provided by the measured strengths of the CO and H_2O absorption features present in modest resolution K -band and H -band spectra. The technique, described in §3, is calibrated using a sample of comparison stars with known T_{eff}

and M_{bol} , selected from the literature to match the T_{eff} and M_{bol} of the GC stars. After T_{eff} and M_{bol} are determined for the GC stars, we place the GC stars in the HR diagram (§4.1) and use this to constrain the star formation history (SFH) within the central few pc of our Galaxy. The SFH calculation is described in §4.2 and discussed in §5. A brief summary is given in §6.

2. OBSERVATIONS AND DATA REDUCTION

Spectroscopic observations of the comparison and GC stars were made using the facility IRS and OSIRIS² spectrometers mounted on the Cerro Tololo Interamerican Observatory (CTIO) 4m Blanco telescope over several runs beginning in 1997 and ending in 2000 (see Tables 1 and 2). In addition, comparison stars were observed at the Michigan–Dartmouth–MIT (MDM) 2.4m telescope on Kitt Peak using the Ohio State University MOSAIC infrared camera/spectrometer (Table 1). The IRS, OSIRIS, and MOSAIC are described by DePoy et al. (1990), DePoy et al. (1993), and Pogge et al. (1998), respectively. The IRS employed a $0.7'' \times 12.5''$ slit, OSIRIS a $1.2'' \times 30''$ slit, and MOSAIC a $0.6'' \times 150''$ slit. The detector pixel scales are $0.32'' \text{ pix}^{-1}$, $0.40'' \text{ pix}^{-1}$, and $0.30'' \text{ pix}^{-1}$ for the IRS, OSIRIS, and MOSAIC, respectively. The IRS and OSIRIS were used in cross–dispersed mode giving essentially full coverage of the J , H , and K bands. MOSAIC was used in JHK grism mode ($1.22 \mu\text{m}$ to $2.29 \mu\text{m}$, where the $2.29 \mu\text{m}$ cutoff is due to the JHK blocking/order sorting filter). For the MOSAIC spectra, an extra, independent K –band segment was obtained for each star covering the red portion of the K –band. This was accomplished using the same setup, but with a K filter instead of the JHK blocker. The spectral resolutions are approximately $\lambda/\Delta\lambda = 1200$, 560, and 750 for OSIRIS, the IRS, and MOSAIC, respectively.

Observing conditions varied over the course of different observing runs. Data were obtained in photometric and non–photometric conditions. The K –band seeing at the CTIO 4m was typically between $0.5''$ and $1''$. At the MDM 2.4m no effort was made to keep the bright comparison stars in good focus, and in fact, sometimes the telescope was intentionally defocused (see below).

All basic data reduction was accomplished using IRAF³. Each spectrum was flat–fielded

²OSIRIS is a collaborative project between the Ohio State University and CTIO. OSIRIS was developed through NSF grants AST 9016112 and AST 9218449.

³IRAF is distributed by the National Optical Astronomy Observatories, which are operated by the Association of Universities for Research in Astronomy, Inc., under cooperative agreement with the National Science Foundation.

using dome flat field images and then sky subtracted using a median combined image formed from the data themselves or from a set of independent sky frames obtained off the source (for the GC stars, typically on dark clouds $\sim 30''$ to $90''$ away). Nearby sky apertures ($\sim 1\text{--}2''$ on either side of the object) were defined on the long slit images and used to correct for over/under subtraction of the night-sky OH lines and the unresolved background light in the case of the GC stars. For the comparison stars, the situation varied depending on the brightness of the star. Some of the stars had to be defocused and/or placed on the edge of the slit in order not to saturate the detector. In a number of cases at the 4m Blanco telescope, the mirror covers were partially closed. These procedures typically produced considerable wings to the PSF. For the IRS, the slit was not long enough in such cases to provide blank sky, so sky frames were obtained off the source, some $5''$ to $10''$ away. These special procedures do not affect the spectral resolution as confirmed by comparing the night sky line widths with similar spectra taken under normal conditions.

Following sky subtraction, the object spectra were extracted from the long slit images by summing the dispersed light over $\pm 3\text{--}5$ spatial pixels (depending on seeing and source crowding in the GC) and then divided by the spectrum of an O, B, or A star to correct for the telluric absorption. For the case of the bright comparison stars which were defocused, the extraction apertures were up to approximately ± 10 pixels. Brackett absorption features in the telluric standards were “fixed” by drawing a line across the feature from continuum points on either side.

The wavelength dispersion solutions were determined from OH lines observed in the H and K bands and the line positions given by Oliva & Origlia (1992). The wavelength zero point was set by moving the observed position of the CO $2.3\ \mu\text{m}$ bandhead to $2.2935\ \mu\text{m}$ (Kleinmann & Hall 1986).

These spectra were then multiplied by a λ^{-4} spectrum approximating the blackbody curve for the telluric standards. For the GC stars, a correction was made for the interstellar reddening assuming the extinction law given by Mathis (1990) and the derived A_K from BDS96.

3. SPECTRAL CLASSIFICATION

3.1. Description of the Technique

BSD96 used K –band spectroscopic indices for CO and H_2O to provide a two–dimensional classification yielding T_{eff} and M_{bol} for cool, luminous GC stars (following Kleinmann & Hall 1986; see also Ramírez et al. 1997). The CO index is a measure of the strength of the 2.2935

$\mu\text{m } 2-0$ ^{12}CO rotational–vibrational bandhead (Kleinmann & Hall 1986). The H_2O feature is a broad depression of the continuum between the H and K –bands due to myriad blended steam absorption lines. There are similar steam absorption bands between the J and H bands and between the K and L bands (Strecker, Erickson, & Witteborn 1978). The latter band can affect the CO bandhead region for stars with extreme H_2O absorption strength (see Sec. 3.2.1). The combination of H_2O and CO features has been used in the past to break the degeneracy in luminosity class and T_{eff} vs absorption strength which exists for each feature alone (see the extensive discussion in Kleinmann & Hall (1986) and BSD96). The correlation of band strength with luminosity is positive for CO (CO increases in stars of higher luminosity) and negative for H_2O (H_2O decreases for stars of higher luminosity).

Several improvements have been made in the present work, relative to the analysis in BSD96. Both H and K band coverage are used to define the H_2O absorption where as BSD96 had only K –band spectra. In that case, the derived H_2O strength was sensitive to the interstellar extinction and reddening for any given star since the relative depression of the blue end of the K band depends sensitively on A_K and the assumed wavelength ($\lambda^{-1.7}$) dependence of the reddening law. Using both H and K –band spectra, the H_2O absorption is seen as a broad “feature” spanning the blue end of the K band and the red end of the H band (as well as a downturn in stellar flux at the blue end of the H band and the red end of the K band). By combining spectra of both the H and K bands, in continuum regions which are not affected by stellar steam absorption, the intrinsic stellar steam absorption at $2.07 \mu\text{m}$ can be distinguished from the interstellar reddening which produces a monotonic decrease in flux toward bluer wavelengths. In the present paper, the CO vs T_{eff} relation has also been improved, placing it on a more quantitative basis which relies less on spectral types and more on T_{eff} measurements. In terms of sample size, we are presenting a GC sample more than three times larger than the one presented by BSD96. A larger sample is crucial for constraining the SFH through theoretical models.

The CO index is defined (BSD96) as the percentage of flux in the CO $2.3 \mu\text{m}$ feature relative to a continuum band centered at $2.284 \mu\text{m}$ ($[1 - F_{\text{band}}/F_{\text{cont}}] \times 100$). The CO band and continuum band were $0.015 \mu\text{m}$ wide and the CO band was centered at $2.302 \mu\text{m}$. The CO index is only marginally affected by extinction since the CO and continuum bands are closely spaced. A typical CO strength of 20% changes by about 1% for a change in A_K of one magnitude. This is similar to the typical uncertainty in the derived CO strength which is taken as the one- σ uncertainty in feature strength derived from the pixel-to-pixel variation in the nearby continuum. The CO and associated continuum band are graphically represented in the *upper* panel of Figure 1⁴.

⁴The data at wavelengths between 1.80 and $1.92 \mu\text{m}$ have been omitted from the plots in Figures 1 and

The H_2O strength is defined similarly to the CO index, but with a quadratic fit to the continuum using bands at 1.68–1.72 μm and 2.20–2.29 μm (see the *lower* panel of Figure 1) and a band 0.015 μm wide centered at 2.0675 μm (indicated in the *lower* panel of Figure 1). The difference between this index and that used by BSD96 is that the latter index used the same continuum band as the CO index (hence the sensitivity in that work to the adopted extinction for any given star). The formal uncertainty in the H_2O strength measured here is a fraction of a percent; the actual uncertainty, 3%, is derived from the scatter of H_2O measurements for supergiants, which have no measurable H_2O . Small changes in the choice of continuum bands used for the fits can lead to systematic changes in the derived H_2O strength of $\lesssim 5\text{--}10\%$, but these tend to affect all the spectra similarly. The systematic uncertainty should be much smaller than that given by BSD96 since the continuum fit spans the *H* and *K* bands and is thus insensitive to the details of the reddening.

3.2. Comparison Stars

The comparison star list is given in Table 1. These stars were chosen to span the range of expected GC star M_{bol} and T_{eff} (BSD96; Carr et al. 2000; Ramírez et al. 2000). The literature was surveyed for cool giant, AGB, and cool supergiant stars with derived T_{eff} and M_{bol} . References for these two quantities are given in Table 1. In addition, we have used five digital spectra previously presented by BSD96 and Lançon & Rocca-Volmerange (1992) for several comparison stars which we were not able to re-observe (see Table 1) but which met our criteria on M_{bol} and T_{eff} . We observed two stars (FL Ser, Z UMa) which we later removed from our sample because they had discrepant T_{eff} compared to stars of similar spectral type (Dyck, van Belle, & Thompson 1998).

3.2.1. CO Index

The comparison stars were used to define a CO index vs. T_{eff} relation which we then used to determine the T_{eff} of the GC stars (see below). In order to produce a relationship between CO and T_{eff} , comparison stars were selected with fundamental, e.g. Dyck et al. (1996), T_{eff} determinations, or T_{eff} determined from detailed spectroscopic analysis. Unfortunately, the list of such stars matching the GC T_{eff} range and also with M_{bol} determined was too small (only four supergiants). Thus, for a number of stars in Table 1 the T_{eff} vs spectral type relation of Dyck et al. (1998) was used to extend our sample of comparison stars (mainly

3,4,7–10 due to the low telluric transmission in these regions.

for the supergiants). A small offset in T_{eff} (-400 K for K type stars, and -220 K for M type) was made for supergiants (Dyck et al. 1996). T_{eff} as determined from the relationship in Dyck et al. (1998) was substituted for two stars whose independent T_{eff} published in the literature gave substantially larger residuals relative to the derived CO vs T_{eff} relationship (3 Cet, Luck & Bond 1980, and CD-60 3621, Luck & Bond 1989).

Following Dyck et al. (1996), two stars of luminosity class II were treated as giants (XY Lyr and π Her), and this is consistent with their measured CO values compared to similar stars of the same spectral type. Conversely, HD163428 (luminosity class II) was included in the supergiant category as its CO is consistent with that group. We made analogous assignments for the S-stars shown in Table 1 which have no luminosity class given explicitly. In all cases, the associated M_{bol} is consistent with the luminosity class chosen, though there is overlap between luminous giants (AGB stars) and less luminous supergiants (see the extensive discussion in BSD96).

The tabulated T_{eff} and computed CO indices for the comparison stars (see Table 3) were used to derive a linear relationship for T_{eff} vs CO strength. The relationship (a least squares fit to the data) is shown for both giants ($T_{\text{eff}} = 4828.0 - 77.5 \times \text{CO}$) and supergiants ($T_{\text{eff}} = 5138.7 - 68.3 \times \text{CO}$) in Figure 2. The offset between the two luminosity classes is due to the effects described in Kleinmann & Hall (1986) and BSD96. Figures 3 and 4 show several supergiant and giant spectra from our sample.

The four points for LPVs shown in Figure 2 effectively constitute a third relationship for T_{eff} vs CO strength; however, the CO strength vs T_{eff} for LPVs does not correlate in the same way as for giants and supergiants (increase in CO strength for lower T_{eff}). This is most likely due to the fact that there is such strong H_2O absorption in these stars that the CO continuum band near $2.29 \mu\text{m}$ is affected (depressed); see Figures 1 and 2. The coolest LPVs have weaker CO. We discuss the determination of T_{eff} for the LPVs in the next section.

3.2.2. H_2O Index

Given a measured CO strength, T_{eff} can be determined using the calibration from the comparison stars (Figure 2), provided the luminosity class is known. For purposes of determining M_{bol} , we take “LPV” as a distinct luminosity class because we assign different bolometric corrections to giants (AGB, III), supergiants (I), and LPVs (Miras, tip of the AGB).

The H_2O strengths for our comparison stars are generally small for both the giants and supergiants because the giants are dominated by earlier M spectral types (a consequence of

our M_{bol} and T_{eff} selection), and the supergiants do not exhibit strong H_2O as described above. H_2O strengths are given in Table 3 for the comparison giants and supergiants. The quoted uncertainty is derived from the scatter of all the giant and supergiant stars. The LPV comparison stars, on the other hand, exhibit strong H_2O absorption, 32 % on average for the four stars listed in Table 3.

For purposes of classification, we will assume the H_2O strengths of late M stars on the AGB lie between those for giants and LPVs. We take the H_2O strength of R Ser ($\text{H}_2\text{O} = 15\%$) to be the lower bound for stars which are likely to be LPVs; see Figure 5. This star is classified as a Mira (i.e. LPV) but has less H_2O absorption than the other luminous LPVs in our sample. Thus any star with $\text{H}_2\text{O} > 15\%$ in the GC will be classified as an LPV candidate. Table 3 shows that T_{eff} depends on the H_2O index for LPVs, in the sense that H_2O is stronger for cooler stars. We use this relationship ($T_{\text{eff}} = 2893.0 - 8.8 \times \text{H}_2\text{O}$) to derive T_{eff} for GC stars which are likely to be LPVs based on their H_2O strength. LPVs are assigned an uncertainty in T_{eff} based on the full range of values for the comparison stars (± 200 K).

For non-LPVs in the GC, the relations between CO and Teff for giants and supergiants, illustrated in Figure 2, are used to derive T_{eff} . The distinction between giants and supergiants, however, is not entirely straightforward. The classifications were initially made by eye, paying attention to the appearance or absence of H_2O between the H and K bands for a given CO strength. However, we then determined what quantitative values of CO, H_2O and M_{bol} reproduced our classifications by eye. We used M_{bol} to make an initial distinction (see §4.1 for the derivation of M_{bol}): GC stars with $M_{\text{bol}} < -7.2$ must be supergiants (see discussion in BSD96), while GC stars with $M_{\text{bol}} > -4.9$ (the faintest M_{bol} known for supergiants; see Table 1 and BSD96) are likely to be giants. The GC stars with $-4.9 > M_{\text{bol}} > -7.2$ could be either giants or supergiants, based solely on M_{bol} .

For the GC stars with $-4.9 > M_{\text{bol}} > -7.2$, we use a combination of CO and H_2O to distinguish giants from supergiants. This is shown in Figure 6. Supergiants have $\text{CO} > 20\%$, and a linear relationship between H_2O and CO defining the upper envelope of supergiants, such that $\text{H}_2\text{O} < -5 + (0.5 \times \text{CO})$, between CO indices of 20 % and 26%, for supergiants. Giants are all the remaining GC stars which have not previously been classified as LPVs or supergiants by these techniques. The bolometric correction (§4.1) depends on assigned luminosity class, and most of the giants with $M_{\text{bol}} > -4.9$ could be more luminous than $M_{\text{bol}} = -4.9$ if the luminosity class was assumed originally to be supergiant instead. However, each case would then result in a giant classification based on the linear relation between CO and H_2O . Thus, the original assignments based on the appearance of H_2O are consistent with the assignments based on the measured CO, H_2O , and derived M_{bol} . For

stars in common with BDS96, we have arrived at the same luminosity classes, and also for star VR5–7 of the Quintuplet cluster. Moneti et al. (1994) classified as VR5–7 as a late-type M supergiant.

As an aside, we note that for two of the comparison stars (R Dor and EP Aqr), we could not compute reliable H₂O indices owing to possible low-order variations and/or slope changes in the continuum. This may be due to the non-standard data taking procedures which were used to keep these bright stars from saturating (see above) although most of the stars appear to have normal spectra independent of how they were obtained. These variations should not affect the relatively narrow and closely spaced CO and associated continuum measurements. R Dor and EP Aqr are the two coolest giants not identified as Miras or LPVs in our sample, yet our spectra show no evidence of H₂O absorption when fit for a continuum like the other stars.

3.3. Galactic Center Sample

The GC stars are listed in Table 2. The complete GC sample was chosen as all stars in the GC K -band luminosity function (KLF, taken here to be the *dereddened* luminosity function) as derived by BDS96 which have $K_{\circ} \leq 7.0$ (where K_{\circ} is the dereddened K magnitude). We have revised several stars to K_{\circ} magnitudes fainter than 7.0 based on new, unpublished H -band images used to determine A_K (see the footnote to Tables 2 and 4). With these adjustments, there are 136 stars in the complete sample. However, 22 stars in this original list were not observed because of severe crowding with neighboring stars, and we were unable to observe an additional 24 stars because of cloudy weather at the telescope. Eleven stars in the list are known emission-line stars or have featureless continua (BDS96, Tables 2 and 4). The featureless stars are apparently young massive stars which are embedded in ionized gas filaments in the central pc (Tanner et al. 2003). We thus take them to be part of the youngest burst of star formation in the GC. All 136 stars are listed in Table 2. Observation dates and instruments are given for the stars for which we obtained new spectra.

Table 5 indicates the level of completeness in the spectroscopic sample as a function of luminosity. In what follows, we assume the stars in our complete list which we were not able to observe are distributed in the Hertzsprung–Russell Diagram (HRD) like the cool stars we have observed. This is a good assumption since previously known emission-line objects (apart from those in Table 5) are fainter than $K_{\circ} = 7.0$, and all of the stars we observed in this work from the complete sample were cool stars.

Example spectra of GC supergiant, AGB, and LPV stars are shown in Figures 7+8, 9,

and 10 respectively. The complete sample of cool stars observed at high spectral resolution by Carr et al. (2000) and Ramírez et al. (2000) is shown in these figures, including all stars for which the values of T_{eff} in this paper were used in the abundance analysis of Ramírez et al. (2000).

Table 6 lists the measured CO and H₂O strengths for each GC star. Four stars in our list are taken from BSD96 and have only K band spectra (IRS 1NE, IRS 1SE, OSUC3, and OSUC4). Classifications for three other stars (#’s 170, 173, and 214) were made based only on their K –band spectra because use of the H –band spectra (which was much fainter) in these cases resulted in poor fits for the continuum and hence H₂O indices which were clearly in error.

The GC star luminosity class is given in Table 6 for each GC star. As noted above, any GC star with H₂O > 15 % is classified as an LPV (or candidate, LPV? in Table 6). We retained the classification of LPV for stars IRS 9, IRS 12N, IRS 24, and IRS 28 of BSD96. These are known photometric variables (Haller et al. 1992, Tamura et al. 1996, BDS96, Ott et al. 1999). For LPVs and LPV?s, the average H₂O was 23 % ± 7 %. Twenty (20) GC stars were classified as LPVs out of the spectroscopic sample of 79.

GC stars with lower H₂O were binned into III and I classes based on the appearance (by eye) of the overall absorption between the H and K –bands and also the measured quantities for CO and H₂O as described in §3.2.2: stars with strong CO compared to the comparison I stars can have slightly stronger H₂O and still be classified as I, while stars with less CO must have very low measured H₂O to be classified as I. The GC luminosity class assignments (based only on the H₂O and CO absorption) are consistent with the comparison star luminosities. If we plot the GC and comparison star H₂O vs M_{bol} , we see the GC stars fall along two broad tracks delineated by the comparison stars (Figure 11). To the lower left in this diagram are the warm comparison star III’s. Going vertically at low H₂O are the supergiants. The comparison star LPV’s run generally to the right to larger H₂O absorption and to gradually higher luminosity. The GC I’s follow on or near the comparison I track, while the cooler GC III’s essentially fill the region between the warmer comparison III’s and the cooler comparison LPVs as is expected for cooler III’s high on the AGB. Several GC stars exist where these broad tracks overlap. In each case, the GC star M_{bol} is consistent with the comparison luminosities for the corresponding class. The average H₂O strength for GC stars classified as giants (III in Table 6) was 10 % ± 3 %. For supergiants, the average was 3 % ± 2 %. The GC stars are also well separated between I and III classes in the H₂O vs. CO plot (Figure 6 and consistent with the positions of the comparison stars.

In summary, we used criteria on the appearance and measured strength of H₂O and measured CO strength to assign all GC luminosity classes. We then showed that the GC

assignments, when quantitatively based on CO, H₂O, and M_{bol} reproduced the classifications by eye and are well matched to the parameters of the comparison stars. The GC giants lie at or below the comparison giant luminosities while supergiants always lie above the minimum comparison supergiant M_{bol} . As noted in §3.2.2, the comparison star sample does not include giants later than type M6 as a consequence of our selection based on M_{bol} and T_{eff} : such stars are rare in the solar neighborhood. Nevertheless, the criteria used here for CO and H₂O indicates that such stars exist in larger numbers in the GC as would be expected in this dense stellar environment.

4. RESULTS: DETERMINATION OF THE STAR FORMATION HISTORY

4.1. The Hertzsprung–Russell Diagram

The spectral indices developed in the preceding section allow us to derive bolometric magnitudes and T_{eff} for the GC stars. T_{eff} follows directly from the measured CO index once the luminosity class is chosen (see §2.3). T_{eff} values are given in Table 6. The uncertainty in T_{eff} is derived by propagating the uncertainty in the measured CO strength through the CO vs. T_{eff} relation. This gives an average uncertainty, for all giants and supergiants in the sample, of 184 K. For the 11 stars in common with the sample given by BSD96 (not including the LPVs), we find $\Delta T_{\text{eff}} = 32 \text{ K} \pm 156 \text{ K}$. In addition, our value of T_{eff} for VR5–7 differs from that calculated by Ramírez et al. (2000) by only 74 K. The M_{bol} for a given GC star follows from the intrinsic K_{\circ} magnitude given in Table 2, the distance modulus, and a bolometric correction to the K_{\circ} magnitude. The uncertainty in M_{bol} is the sum in quadrature of the photometric uncertainty (BSD96) and an 0.4 mag uncertainty due to the uncertainty in the interstellar extinction law (Mathis 1990). The distance modulus is taken as 14.52 (8 kpc, Reid 1993).

The bolometric correction (BC_K) is derived from the literature for the different luminosity classes given in Table 6. For supergiants and LPVs (Table 6), the BC_K is the same as given by BSD96: $\text{BC}_K = 2.6$ for supergiants and 3.2 for LPVs. For the giants, we improve on the work of BSD96 by considering a BC_K which is a function of T_{eff} . Using the BC_K as a function of $J - K$ given by Frogel & Whitford (1987), the mean $J - K$ of giants as a function of spectral type from Frogel et al. (1978), the spectral type vs T_{eff} from Ramírez et al. (2000) and Dyck et al. (1998), and the T_{eff} given in Table 6, we derive BC_K as a linear function of T_{eff} ($\text{BC}_K = 2.6 - [T_{\text{eff}} - 3800]/1500$). These BC_K range from 2.8 to 3.2 for the warmest and coolest GC giants.

A second correction was also applied to the GC stellar M_{bol} values which relates to the

A_K for each star. BDS96 used mean $(J - H)_o$ and $(H - K)_o$ colors to estimate the A_K for each GC star. As discussed by them, this will lead to systematically too high A_K for stars which are intrinsically redder than these colors, and the opposite will be true for stars intrinsically bluer. The individual spectrum for each star now allows us to improve upon the corresponding A_K estimate. Using the same color and T_{eff} data described in the preceding paragraph, we estimated a correction (linear with T_{eff}) to the intrinsic colors, and hence to A_K for each star. This correction varied from 0.0 to 0.5 mag depending on T_{eff} (see Table 6) and was applied in the sense which makes A_K less for each star ($\Delta A_K = -0.11 - [T_{\text{eff}} - 3800]/1730$).

Figure 12 shows the HRD for all the GC stars and comparison stars listed in Tables 3 and 6. This figure illustrates that the comparison stars span the same range in M_{bol} and T_{eff} as the GC stars do.

Figure 13 shows the HRD for all the GC stars listed in Table 6, with isochrones from Bertelli et al. (1994) and Girardi et al. (2000) overplotted. These isochrones vary in age from 10 Myr to 12 Gyr, with $[\text{Fe}/\text{H}] = 0.0$ for all ages. Figure 13 shows that our GC sample spans a wide range in age. As can be seen in the Figure, all of the GC giants (those labeled "III" in Table 6) are AGB stars. They are too luminous to be first ascent giants, which is a consequence of our selection criteria.

Figure 14 again shows the HRD for the GC, but this time overplotted with Bertelli et al. (1994) and Girardi et al. (2000) isochrones having $[\text{Fe}/\text{H}] = -0.2$ for all ages. The Figure shows that lower metallicity isochrones do not extend to cool enough T_{eff} to match the GC HRD.

To give a general feel for the SFH represented by Figure 13, Figure 15 shows the HRD against a simulation representing a constant SFH. The observed points appear to span the model parameter space. The relatively few model stars at high and low luminosities suggests that higher star formation rates in both the distant and recent past are needed to fit the data. There is an intermediate age component at $T_{\text{eff}} = 3300$ K, $M_{\text{bol}} = -5.0$ whose position and extent matches the model well. The tightness of this feature suggests that our errors may be over estimated relative to the internal scatter in the points. This is particularly true for the errors in M_{bol} which are dominated by the *systematic* uncertainty in the interstellar extinction law.

One exception in the model coverage appears to be the coolest AGB stars. Both the Bertelli et al. (1994) and Girardi et al. (2000) models fail to reach the coolest observed T_{eff} . This is true of both the GC and comparison stars. Thus, only stars with $T_{\text{eff}} > 2800$ K (allowing for the errors in T_{eff} for the observed stars) were directly included in the basic

SFH calculations discussed below. The models attempt to follow evolution along the AGB in a simplified way (Girardi et al. 2000) giving a typical or average locus in the HRD, but real AGB stars pulsate with periods of 100’s of days. These pulsations result in excursions in the HRD of 500–1000 degrees (Lançon & Mouhcine 2002). As discussed by Lançon & Mouhcine (2002), the effect of pulsations is thus to widen the AGB. For stars which experience excursions within the model temperature range ($T_{\text{eff}} > 2800$ K), the pulsations will be randomly phased, so that differences between the observed location in the HRD and the actual isochrone to which a star would otherwise be associated with are canceled out. For stars which are cooler than the models, we assume they should be associated with an isochrone inside the model HRD space. Assuming that these stars represent the same fraction of initial mass independent of which isochrone they are really associated with, we simply scale the total star formation by their number. In this case, there are 20 such cool stars (out of 78 used to calculate the SFH), thus we will take the total star formation rates to be 1.3 times the amount given by our fit results.

We also did not include IRS 7. This star belongs to the youngest nuclear star burst which is accounted for by the Krabbe et al. (1995) model.

BSD96 estimated ages for a number of the coolest, most luminous stars which are also shown in Figures 12, 13, and 14. The effect of a reduced A_K for these stars (compared to BSD96) has lowered their luminosity. This tends to increase the estimated age. In particular, for IRS 9, 12N, 23, 24, and 28 (see Table 6), BSD96 estimated the mass for these stars from their luminosity. This resulted in correspondingly young ages (100–200 Myr) from model isochrones. The reduced luminosity determined in the present work (due to the decrease in A_K), and comparison to different model isochrones as adopted herein (Figure 13) suggests a somewhat older age for these stars (roughly 500 Myr – a few Gyr). Given the preceding discussion, it is not possible to estimate the age of any particular star to great precision.

4.2. Star Formation History Calculation

We have used the results of Figure 12 to derive the SFH implied by these observations of the GC cool stars. The calculation was carried out using Olsen’s (1999) implementation of the method described by Dolphin (1997), with some modifications. In brief, we constructed a set of models describing the expected distribution of stars in the H–R diagram within specified age bins, assuming a particular metallicity, slope of the initial mass function (IMF), and constant star formation rate ($1 \text{ M}_{\odot}\text{yr}^{-1}$) within the bin and accounting for observational errors and incompleteness. We chose the best model SFH for the GC by fitting the observed data to a linear combination of the star formation within these bins. This fit was determined

through the maximum likelihood analysis described below.

4.2.1. Model Parameters

Two choices of sets of age bins and metallicities were used. Models had either four age bins (Model A, 10–100 Myr, 100 Myr – 1 Gyr, 1–5 Gyr, and 5–12 Gyr) or three age bins (Model 1, 10–50 Myr, 50 Myr – 3 Gyr, and 3–12 Gyr). For both sets of age bins, models were run with all stars at solar $[\text{Fe}/\text{H}]$ (Models A with four age bins and Model 1 with three age bins), and then again with solar $[\text{Fe}/\text{H}]$ for the younger stars and $[\text{Fe}/\text{H}] = -0.2$ in the oldest bin (Model B with 4 age bins, Model 2 with three age bins). To explore the effect of the IMF on the derived SFH, we also computed models with a power-law slope $\alpha = -2.35$ (Salpeter 1955) and with a slightly flatter slope $\alpha = -2$ for stars with masses $> 1M_{\odot}$. The matrix of models is given in Table 7.

The SFH is also constrained by the amount of mass inferred from dynamical models in the GC. Recent models have been computed by McGinn et al. (1989), Sellgren et al. (1990), Haller et al. (1996), Genzel et al. (1996), Saha, Bicknell, & McGregor (1996), Ghez et al. (1998), and Genzel et al. (2000). The most detailed models, which include proper motion and radial velocities (Ghez et al. 1998; Genzel et al. 2000) require a concentrated mass of approximately $3 \times 10^6 M_{\odot}$ (presumably a super massive black hole) which dominates the distribution within less than 1 pc. These models also predict approximately $6 \times 10^6 M_{\odot}$ total mass enclosed within a radius of 2 pc (for $R_{\odot} = 8$ kpc). Finally, new observations of single stars orbiting the black hole (Schödel et al. 2002; Ghez et al. 2003) require slightly higher black hole masses of $\approx 4 \pm 1 \times 10^6 M_{\odot}$.

If the black hole itself was not built up from stars and stellar remnants in the formation of the nucleus, this leaves roughly $1-3 \times 10^6 M_{\odot}$ in distributed mass which arises from the luminous stellar population and the accumulated stellar remnants integrated over the life time of the nucleus.

We built in the constraint on dynamical mass by limiting the low mass end of the IMF. The constraint is taken to be: black hole mass + stellar mass formed – mass loss from stellar winds = total dynamical mass. We discuss the effects of mass loss on the present day mass below in §5. This is the simplest choice since our HRD is not sensitive to stars below about $1 M_{\odot}$. We discuss a possible cause for this low mass cutoff below in §5. We began with the same IMF as Miralda-Escudé & Gould (2000, and including their corrections), with masses spanning the range 0.08–120 M_{\odot} . This IMF is based on Salpeter’s mass function for the more massive stars (Salpeter 1955); i.e. $dN/dM \propto m^{-\alpha}$ with $\alpha = -2.35$. For lower masses,

the IMF is flatter, as determined from bulge star counts at 6° projected distance from the GC (Zoccali et al. 2000, exponent -2.0 for $1 M_\odot > M > 0.7 M_\odot$ and -1.65 for $M < 0.7 M_\odot$). For the lowest masses, there is a correction to the exponent due to binaries (Miralda-Escudé & Gould 2000). In the end, we found that cutting off the mass function at $0.7 M_\odot$ resulted in models which are consistent with the present day dynamical mass.

4.2.2. Model Calculations

Within each age bin, we calculated the distribution of stars over a fine grid in T_{eff} and M_{bol} directly from 20 isochrones spaced linearly in age. We used the Girardi et al. (2000) isochrones to construct the models with ages ≥ 63 Myr and the Bertelli et al. (1994) isochrones for younger models; we interpolated the isochrones in age and metallicity following the procedure described in Olsen (1999). We then convolved the grid with a 2-D Gaussian kernel having a shape representing the typical errors in T_{eff} and M_{bol} and multiplied the grid with a surface representing our estimate of the completeness as a function of T_{eff} and M_{bol} (i.e., the models were transformed to the observational plane).

After gridding the observed H–R diagram to the same resolution as the models and selecting an area to exclude the likely Mira variable stars, we searched for the linear combination of models producing the highest likelihood of describing the observed distribution of stars. This search was done by using the *Numerical Recipes* routine *amoeba* (Press et al. 1992) to minimize the Poisson maximum likelihood parameter $\chi_\lambda^2 = 2 \sum_i m_i - n_i + n_i \ln \frac{n_i}{m_i}$ (e.g. Mighell 1999), where m_i is the number of stars predicted by the model in the i th bin of the H–R diagram and n_i is the number of observed stars in the bin. The virtues of this parameter are discussed extensively by Dolphin (2002)—the most important of which is that it minimizes to the correct solution when presented with a dataset that sparsely samples the range of possible measurements (i.e. the Poisson regime), which the standard χ^2 does not.

4.2.3. Uncertainties and Goodness of Fit

The size of the errors in M_{bol} and T_{eff} , the size of our dataset, and the fact that we are studying only the most luminous members of the GC population impose some limitations on our ability to discriminate model SFHs. First, we selected the age bins so as to roughly divide the H–R diagram into equal areas and to distinctly separate the footprints of adjacent age bins, given our errors. Because the isochrones bunch together at larger ages, the age bins necessarily grow wider with age, with a corresponding decrease in age resolution in

the derived star formation histories. Second, we specified the age–metallicity relation in advance. While the maximum likelihood procedure described above in principle has the ability to *derive* the metallicity distribution and age–metallicity relation directly from the data, the degeneracy between age and metallicity in this region of the H–R diagram is severe. This difficulty is compounded by our sizable errors in M_{bol} and T_{eff} and the relatively small size of our sample. Finally as mentioned above, we assumed the IMF, since our data do not span a large enough range in mass at a given age to allow it to be a free parameter.

For each model in Table 7, we calculated the uncertainties in the derived star formation rates through Monte Carlo simulations. We produced 100 Monte Carlo samples, each containing 59 stars, by drawing randomly from the *observed* dataset while allowing any particular star to be drawn any number of times (a technique referred to as “bootstrapping”). For each sample, we then derived the star formation history just as was done for the original dataset. The uncertainty in a given star formation rate (σ_{SFR}) reported in Table 7 is the $1-\sigma$ standard deviation of the distribution of star formation rates in the corresponding age bin for the 100 Monte Carlo samples.

To address the separate question of whether the data are a likely representation of the models listed in Table 7, we ran a different set of Monte Carlo simulations. For these simulations, we produced 10000 samples, each containing 59 stars drawn randomly from the *fitted* models (*not* from the *data*). We then assembled the distribution of minimum values of the χ^2_λ parameter by re-fitting the model to each Monte Carlo sample. The column labeled P_λ in Table 7 shows the percentage of runs that had higher χ^2_λ when fitting the Monte Carlo sample to the model than that obtained by a fit of the data to the model. Thus, small values of P_λ represent poorer fits of the models. This is so because Monte Carlo samples drawn from the “right” model should, on average, produce as many fits with χ^2_λ above as below that for the fit to the data: values near 50% are achieved by the average dataset drawn randomly from the model probability distribution.

4.2.4. Model Results

Examining Table 7, we find that the models with only three age bins are significantly worse than those with four, and so are not discussed further. Model A, in which we assume solar metallicity throughout, exclude the coolest stars and the most luminous one, and account for the uncertainty in the extinction law, fits the data as well as it does the average dataset drawn randomly from the model. Model B, which is identical to Model A except that we assume $[\text{Fe}/\text{H}] = -0.2$ for ages >5 Gyr, is an unlikely fit to the data.

As suggested by Figures 13 and 14, age and metallicity are difficult to disentangle using only the tip of the AGB. However, our models do produce better fits to a SFH with purely solar $[\text{Fe}/\text{H}]$ from 0.01–12 Gyr. This may be understood through consideration of Figure 16. The *left* panel shows Model A compared with the data, while the *right* panel shows Model B. The colors cyan, magenta, yellow, and gray represent the model distributions scaled to the best-fit SFR. Darker regions indicate higher number density of stars. In the case of Model A, the footprints of the different age bins align nicely with concentrations of observed data points. In Model B, the oldest age bin moves to higher temperature and luminosity, becoming degenerate with the solar metallicity, younger stars and forcing it to fit a larger number of points. As a result, Model B does not fit the coolest low luminosity stars well; indeed, these stars are difficult to fit with anything other than a > 12 Gyr old solar metallicity model. However, > 12 Gyr-old stars with $[\text{Fe}/\text{H}] \lesssim -0.6$ are less luminous than our T_{eff} -dependent M_{bol} limit. This means our SFH may not account for a potential very old (> 12 Gyr old), metal-poor component which might have fewer luminous AGB stars.

The resulting SFH for Models A&B, showing the SFR in age bins of 10–100 Myr, 100 Myr – 1 Gyr, 1–5 Gyr, and 5–12 Gyr, are given in Figures 17 and 18, respectively. The total initial mass represented by these SFHs are shown in Figures 19 and 20, respectively. In Figure 17, we have also plotted a point corresponding to the model of Krabbe et al. (1995) which we take as the average SFR over the last 10 Myr based on their burst model which produces approximately $3200 M_{\odot}$.

5. DISCUSSION

A number of investigators have discussed the SFH in the GC. Lebofsky et al. (1982a) used the presence of young M supergiants to infer a recent ($\lesssim 10$ Myr) burst of star formation. Sellgren et al. (1987) later re-classified some of the same stars used by Lebofsky et al. (1982a) as luminous AGB stars, indicating intermediate ages ($\gtrsim 100$ Myr) were present as well. Genzel, Hollenbach, & Townes (1994) discussed the SFH in terms of a constant SFR and noted that such a model produces too few young blue supergiants if it is adjusted to match the number of older late-type stars. Krabbe et al. (1995) modeled the most recent epoch of star formation in the nuclear cluster, producing the observed blue supergiants with a burst of $10^{3.5} M_{\odot}$ over the last ~ 7 Myr. This point is shown in Figure 17. Apparently, the GC is currently in a more quiescent state than in the recent past. Davidge et al. (1997) argued for an old population to dominate the number counts within $6''$ (0.23 pc) of the nuclear cluster based on near infrared photometry. Philipp et al. (1999) used surface brightness fitting and photometry of individual stars to discuss the relative contributions of young and old stars

over a larger ($\sim 11' \times 11'$) area. Mezger et al. (1999) used the same data presented by Philipp et al. (1999) to further constrain the star formation history. Recently, van Loon et al. (2002) used photometric spectral energy distributions of a large sample of stars in the Galactic bulge to investigate the stellar populations there. Their results are qualitatively similar to those presented here, though they investigate a much larger area and have poor angular resolution in the central few pc. BSD96 used near infrared spectra similar to those presented here to identify young, intermediate age, and old stars. In the present paper, we build on this earlier work by computing the SFH directly from the observed stars using the M_{bol} and T_{eff} determined from the individual stellar spectra.

5.1. Stellar Remnants

Some fraction of the mass within the GC is due to massive stellar remnants (neutron stars or black holes from initially massive stars) which have migrated there from further out (Morris 1993; Miralda-Escudé & Gould 2000) by dynamical friction with the low mass stellar population. To the extent that some of these massive objects were formed outside the 2 pc radius covered by our data, that mass is unaccounted for in our SFH model. Morris (1993) has computed migration times as a function of mass and finds a remnant of $10 M_{\odot}$ could migrate in to the center from about 4 pc radius in a Hubble time. Miralda-Escudé & Gould (2000) find a similar result. The most massive remnants, black holes, will be able to migrate inward from the largest radius. Their large mass and volume over which they are drawn mean they will dominate this extra mass component (Morris 1993).

Morris (1993) explored a range of models and found that up to $\sim 10 \times 10^6 M_{\odot}$ in massive remnants might have migrated by dynamical friction to the central pc (Morris' models for similar IMFs as used here produce masses $\lesssim 5 \times 10^6 M_{\odot}$). This mass, which lies within a radius of 0.8 pc, overestimates the dynamical mass including the central black hole for the most detailed models mentioned above (by about a factor of two). Miralda-Escudé & Gould (2000) estimate that 25,000 $7 M_{\odot}$ black hole remnants could have settled in the central pc over a Hubble time; these remnants would still be in the stellar cluster because the depletion timescale for capture by the central black hole is 30 Gyr. Given the somewhat lower estimate of remnant mass due to migration by Miralda-Escudé & Gould (2000) and the estimate of $\sim 2 \times 10^6 M_{\odot}$ in a luminous stellar cluster by Schödel et al. (2002) within a 2 pc radius of the center, we expect on order of at least a few times $10^6 M_{\odot}$ in stars to have formed in the inner 2 pc radius. If the Galaxy is 10 Gyr old, then this implies a time averaged SFR of $\gtrsim 2 \times 10^{-4} M_{\odot} \text{ yr}^{-1}$.

5.2. Depletion of CO Absorbers in the Central Parsec

Sellgren et al. (1990) showed that the CO absorption strength seen through apertures centered on *unresolved* starlight was weaker inside a radius of $15''$ (0.58 pc) than outside this radius; see also Genzel et al. (1996). We now know the weakness of the CO feature is due in part to dilution by very young stars (Genzel et al. 1996, for example). Genzel et al. (1996) also showed that the brightest resolved sources with strong CO (i.e. luminous AGB stars or supergiants) were absent from the inner $5''$ (0.19 pc). Both Sellgren et al. (1990) and Genzel et al. (1996) concluded it was possible that the atmospheres of such stars might be destroyed by collisions with lower mass stars in the GC leading to a deficiency of CO-strong stars. Bailey & Davies (1999) made detailed calculations of collision probabilities in the GC and concluded that collisions between giants and lower mass stars was unlikely to explain the putative missing stars because such collisions (which form a common envelope system) were ultimately ineffective in expelling the giant’s envelope on a time scale shorter than the evolutionary time scale. However, Davies et al. (1998) did find that collisions between giants and *binaries* might be effective in removing the giant atmospheres in a short enough time to be observable (again through the development of common-envelope systems). In any case, the deficiency of resolved AGB or M supergiant stars is actually well concentrated to the center (Genzel et al. 1996, $R \lesssim 5'' = 0.2$ pc) and should thus not affect the SFH estimates for the larger area studied in this work ($R \sim 2'$).

A consequence of the migration of massive remnants into the central pc is the relaxation of the resulting dark cluster with the lower mass stars which exist there. The model of Miralda-Escudé & Gould (2000) predicts that stars older than a few Gyr will be pushed to larger radii, forming a distribution with a larger core radius (1–2 pc) and lower core density than they would otherwise have. The implication of this prediction is that the present data set would not be sensitive to the oldest epochs of star formation in the GC if a significant fraction of the $\sim 1 M_{\odot}$ tracers have been removed from the inner 2 pc, and so might underestimate the total SFH. On the other hand, if the extent of the dynamical redistribution of the low mass stars is toward the low end of the range predicted by Miralda-Escudé & Gould (2000, core radius ~ 1 pc) then we would not expect this to be a large effect. The total amount of mass deduced from dynamical models also constrains the SFH, and we discuss below the possibility that this constraint coupled with our models may provide evidence that the dynamical friction effects are seen in the GC.

5.3. The Star Formation History

Figure 17 indicates significant on-going star formation in the central few pc, but that the bulk of stars (roughly 75 % by mass) formed at earlier times (Figure 19). This is in agreement with earlier work based on near infrared number counts (Genzel et al. 1994; Mezger et al. 1999), and for the range of parameters discussed in §3 and listed in Table 7, this conclusion holds. For the oldest stars, we are sampling just the very tip of the AGB, hence to observe any stars in such a short lived phase requires a large mass to have originally formed. The details change by roughly \sim a factor of two depending on which model SFH is chosen. The goodness of fit criterion, P_λ , suggests the uniform metallicity case (Model A) is preferred. If true, it could suggest that the nucleus formed largely from enriched material produced in the early formation of the bulge. The purely solar $[\text{Fe}/\text{H}]$ is also consistent with the narrow distribution of $[\text{Fe}/\text{H}]$ from high resolution spectra (Ramírez et al. 2000). Though the range of ages considered by Ramírez et al. (2000) is not as large as the data set presented here, the high resolution data sample stars with ages up to ~ 5 Gyr (Figure 13). In §3, we noted that the current data set may not be sensitive to metal poor populations older than 12 Gyr.

The total mass represented by the SFH in Figure 17 is shown in Figure 19 and is $9.9 \pm 3.0 \times 10^6 M_\odot$ for Model A. This is about three to six times larger than the most detailed models (not counting the central black hole mass).

However, mass loss during the lifetime of stars from about one to $120 M_\odot$ will reduce the cumulative final mass in the cluster. If all stars with $120 M_\odot > M > 1 M_\odot$ are taken to have their remnant mass at the present time, then, using the mapping of initial mass to final mass given by Morris (1993), the present mass in stars is reduced by about 68 % (i.e. we infer the present mass in stars remaining in the cluster to be $0.32 \times$ the total mass formed over all times) to a total of $3.2 \pm 1 \times 10^6 M_\odot$ which is consistent with the dynamical models cited in §4.2.1. The total present day mass from the SFH depicted in Figure 17, but including mass loss, is shown in Figure 19. We have implicitly assumed all the tracers of the SFH lie within a true radius of 2 pc, but they are actually distributed in a projected radius of 2 pc. Given the steepness of the stellar cluster radial density distribution ($\lesssim 0.5$ pc core radius), the overestimate is likely to be small. The mass lost through stellar winds could be expelled from the region and/or recycled into new generations of stars. This is the maximal mass loss since not all stars are yet old enough to have reached their final mass, though most of the star formation has occurred at earlier times.

Morris (1993) argued that the IMF in the CMZ should be slanted toward higher masses than the Salpeter (1955) mass function. Figer et al. (1999) derived a flatter mass function in the nuclear young cluster, the Arches, 30 pc from the GC. However, it is not clear if this is representative of the initial mass function or dynamical effects (Portegies Zwart, Makino,

McMillan, & Hut 2002). An IMF slanted toward higher masses increases the total mass derived here since the IMF must still produce the same number of low mass stars which form the majority in Figure 13. For the same low mass cut-off of $0.7 M_{\odot}$, the flatter IMF model yields a total mass of $16.4 \pm 5.2 \times 10^6 M_{\odot}$. This model loses more mass through stellar winds resulting in a present day mass of $3.9 \pm 1.2 \times 10^6 M_{\odot}$. This is not too different than Model A discussed above. Higher values of the lower mass cut-off can reduce the total mass formed and thus the present day mass, but the cut-off is already near the limit of the mass of stars which we observe in the HRD (about $1 M_{\odot}$). Apart from this, our models are not very sensitive to the details of the IMF.

Our derived SFH may provide evidence that a significant number of low mass stars have been removed from the central few pc as suggested by Miralda-Escudé & Gould (2000). Our models, which trace the initial mass formed, require that we cut-off the lower end of the mass function (below $0.7 M_{\odot}$) in order to produce a final mass which is consistent with the dynamical mass in central few pc. It is possible that this mass is actually formed, but subsequently removed by dynamical friction as massive remnants migrate toward the center (Morris 1993; Miralda-Escudé & Gould 2000). A better test of the dynamical relaxation effect predicted by Miralda-Escudé & Gould (2000, as they point out) is to compute the radial distribution of the many fainter low mass stars. Alternately, the cut-off at $0.7 M_{\odot}$ may represent a bias to higher masses forming in the GC as argued by Morris (1993) and Figer et al. (1999).

Our technique of deriving M_{bol} and T_{eff} from low resolution spectra is preferred over broad-band photometric analyses because of the large scatter in A_K in the GC (BDS96) and the large variation in intrinsic colors of the giant stars (which can be corrected for with the spectroscopically derived T_{eff}). Newly commissioned multi-object infrared spectrometers on large telescopes are now available and will be used in the near future to make these observations. Obtaining such observations to 1.5–2 mag deeper than present will also improve the SFH calculation (e.g., Figure 15) as the lower parts of the older isochrones will be more densely populated. The observational errors on T_{eff} and M_{bol} still set a limit on the final age resolution, however.

Our sample includes a number of luminous stars which require a substantial amount of very recent star formation (10-100 Myr). The high star formation rate at later times is reflected in Figure 17 and Figure 15. The relatively large number of luminous AGB and supergiant stars in this region of the HRD requires significant recent star formation, perhaps in the form of one or more concentrated bursts. Another way to see this is by considering Figure 15. There is a relative paucity of luminous stars in the part of the HRD covered by the youngest isochrones for a constant star formation rate compared to the cooler, less

luminous AGB stars. Our models do not rule out high SFRs at early times (in concentrated bursts); the lower mean SFRs result from the wider age bins. The SFR in the youngest (and narrowest) age bin is similar to the in fall rate of gas into the 2 pc molecular ring (see §1). This suggests star formation might be relatively efficient in the GC ($\sim 50\text{--}100\%$), though the current SFR from Krabbe et al. (1995) is a factor of 10 lower than in our most recent bin.

In §1, we noted that the CMZ was forming about $0.5 M_{\odot} \text{ yr}^{-1}$. If we consider the SFR in the CMZ and GC per unit area (taking a 200 pc radius disk-like distribution for the CMZ), then the GC has formed stars at a prodigious rate over its history. The CMZ normalized SFR is $4 \times 10^{-6} M_{\odot} \text{ yr}^{-1} \text{ pc}^{-2}$. In the GC, the average SFR is $\sim 8 \times 10^{-4} M_{\odot} \text{ yr}^{-1}$, and taking a radius of 2 pc, gives $6 \times 10^{-5} M_{\odot} \text{ yr}^{-1} \text{ pc}^{-2}$ with a peak of $2.6 \times 10^{-4} M_{\odot} \text{ yr}^{-1} \text{ pc}^{-2}$.

Sjouwerman et al. (1999) have used luminous OH/IR (maser sources) stars as tracers of star formation on larger scales (up to 50 pc) in the GC region. They find evidence of significant star formation at an epoch $\gtrsim 1$ Gyr ago. Narayanan, Gould, & DePoy (1996) and Wood, Habing, & McGregor (1998) also find evidence for massive AGB, hence intermediate age, stars indicating significant star formation on a similar time and spatial scale. Frogel et al. (1999) studied the K -band number counts of stars in the inner Galaxy and found that the younger (i.e. intermediate age) population may extend out to a degree from the nucleus. There is a feature in the HRD of Figure 13 which coincides with this age range. It is the relatively dense group of stars centered at $T_{\text{eff}} = 3300$ K, $M_{\text{bol}} = -5.0$. This feature represents significant intermediate age star formation ($\sim 1\text{--}2$ Gyr), though not a significant fraction of the total mass. The number of stars which trace out tracks near 1 Gyr in Age is suggestive of a true “burst,” though our models do not have the time resolution to conclusively limit the duration of this star formation activity. van Loon et al. (2002) have discussed the properties of the stellar populations in the inner Galaxy using broad-band photometric indices from the DENIS and ISOGAL surveys. These surveys, whose angular resolution is more appropriate for studies on large scales, give results which are broadly consistent with those presented here. In particular, they find that the bulk of stars in the inner Galaxy are old and not metal poor, that there has been significant star formation at intermediate ages, and that current star formation rates are relatively high. The correspondence of star formation tracers in the central parsecs and on larger scales suggests that star formation in the GC may be influenced by processes in the inner Galaxy at large. The supply of gas to the central few pc may be linked to the stellar bar which is thought to be a mechanism to funnel star forming material to the inner Galaxy (see §1).

6. SUMMARY

We have presented a Hertzsprung–Russell diagram (HRD) for a sample of 79 cool and luminous M type stars in the central few pc of the Galaxy. The sample is based on a magnitude limited K –band data set presented by Blum et al. (1996a). The T_{eff} and M_{bol} were derived from CO and H₂O molecular absorption features in $\lambda/\Delta\lambda \sim 550 - 1200 H$ and K –band spectra.

The HRD was used to derive the star formation history for the Galactic center. Our sample of stars is too small to independently constrain all the parameters in a detailed SFH (e.g, the slope of the initial mass function, and the chemical enrichment history), thus our SFH is not strictly unique. However, we find that the bulk of stars in the Galactic center formed at early times ($\gtrsim 5$ Gyr ago) for a range of model parameters. There is also evidence for significant recent star formation (\lesssim few Gyr ago). Such recent star formation activity coincides in time with evidence from other evolved stars at larger radii in the inner Galaxy (> 50 pc), and suggests a connection between star formation in the central pc and on larger scales (presumably through gas input to the region). The age resolution of our sample is not great due to observational errors on the derived M_{bol} and T_{eff} , the fact that the oldest isochrones are not well separated along the asymptotic giant branch, and the relatively small number of old, luminous stars, which trace the majority of the derived mass. Our best fitting models require a cut–off in the IMF below a solar mass (at $\sim 0.7 M_{\odot}$) in order to produce a present–day mass in the central few pc which is consistent with existing enclosed masses derived from dynamical models. This “cut–off” might be evidence that mass segregation effects are at work in the GC, as has been predicted previously, or might instead point to a bias towards high mass star formation. Finally, we find better fits to the data with models which have $[\text{Fe}/\text{H}]=0.0$ at all ages. This is consistent with earlier work at high spectral resolution which showed that stars between 10 Myr and ~ 5 Gyr in the GC have solar metallicity.

SVR and KS gratefully acknowledge support for this project from the NSF through grants AST-9619230 and AST-0206331. This research has made use of the SIMBAD database, operated at CDS, Strasbourg, France. We would like to thank P. Martini, P. Romano, and J. An for helping obtain the observations of Galactic center stars at CTIO and comparison stars at MDM. Finally, we thank an anonymous referee whose comments and criticisms of our paper have led to its improvement.

REFERENCES

- Allen, D. A., Hyland, A. R., Hillier, D. J. 1990, MNRAS, 244, 706
- Bailey, V. C. & Davies, M. B. 1999, MNRAS, 308, 257
- Barthes, D. 1998, A&A, 333, 647
- Becklin, E. E. & Neugebauer, G. 1975, ApJ, 200, L71
- Bedding, T. R. & Zijlstra, A. A. 1998, ApJ, 506, L47
- Benson, P. J. & Little-Marenin, I. R. 1996, ApJS, 106, 579
- Bertelli, G., Bressan, A., Chiosi, C., Fagotto, F., & Nasi, E. 1994, A&AS, 106, 275
- Binney, J., Gerhard, O. E., Stark, A. A., Bally, J., & Uchida, K. I. 1991, MNRAS, 252, 210
- Blum, R. D., Sellgren, K., & DePoy, D. L. 1995*a*, ApJ, 440, L17
- Blum, R. D., DePoy, D. L., & Sellgren, K. 1995*b*, ApJ, 441, 603
- Blum, R. D., Sellgren, K. & DePoy, D. L. 1996*a*, ApJ, 470, 864 (BDS96)
- Blum, R. D., Sellgren, K. & DePoy, D. L. 1996*b*, AJ, 112, 1988 (BSD96)
- Blitz, L. & Spergel, D. N. 1991, ApJ, 379, 631
- Carr, J. S., Sellgren, K., & Balachandran, S. C. 2000, ApJ, 530, 307
- Davidge, T. J., Simons, D. A., Rigaut, F., Doyon, R., & Crampton, D. 1997, AJ, 114, 2586
- Davies, M. B., Blackwell, R., Bailey, V. C., & Sigurdsson, S. 1998, MNRAS, 301, 745
- DePoy, D. L., Gregory, B., Elias, J., Montane, A., Pérez, G., & Smith, R. 1990, PASP, 102, 1433
- DePoy, D. L., Atwood, B., Byard, P., Frogel, J. A., & O’Brien, T. 1993, in SPIE 1946, “Infrared Detectors and Instrumentation,” pg 667
- Dolphin, A. E. 2002, MNRAS, 332, 91
- Dumm, T. & Schild, H. 1998, New Astronomy, 3, 137
- Dwek, E. et al. 1995, ApJ, 445, 716
- Dyck, H. M., Benson, J. A., van Belle, G. T., & Ridgway, S. T. 1996, AJ, 111, 1705

- Dyck, H. M., van Belle, G. T., & Thompson, R. R. 1998, *AJ*, 116, 981
- Elias, J. H., Frogel, J. A., & Humphreys, R. M. 1985, *ApJS*, 57, 91
- Fernandez-Villacanas, J. L., Rego, M., & Cornide, M. 1990, *AJ*, 99, 1961
- Figer, D. F., Kim, S. S., Morris, M., Serabyn, E., Rich, R. M., McLean, I. S. 1999, *ApJ*, 525, 750
- Forrest, W. J., Shure, M. A., Pipher, J. L., & Woodward, C. E. 1987, *AIP Conf. Proc.* 155: The Galactic Center, 153
- Frogel, J. A., Persson, S. E., Matthews, K., & Aaronson, M. 1978, *ApJ*, 220, 75
- Frogel, J. A. & Whitford, A. E. 1987, *ApJ*, 320, 199
- Frogel, J. A., Tiede, G. P., & Kuchinski, L. E. 1999, *AJ*, 117, 2296
- Genzel, R., Hollenbach, D., & Townes, C. H. 1994, *Reports of Progress in Physics*, 57, 417
- Genzel, R., Thatte, N., Krabbe, A., Kroker, H., & Tacconi-Garman, L. E. 1996, *ApJ*, 472, 153
- Genzel, R., Pichon, C., Eckart, A., Gerhard, O. E., & Ott, T. 2000, *MNRAS*, 317, 348
- Ghez, A. M., Klein, B. L., Morris, M., & Becklin, E. E. 1998, *ApJ*, 509, 678
- Ghez, A. M. et al. 2003, *ApJ*, 586, L127
- Girardi, L., Bressan, A., Bertelli, G., & Chiosi, C. 2000, *A&AS*, 141, 371
- Güsten, R. 1989, *IAU Symp.* 136: The Center of the Galaxy, 136, 89
- Güsten, R., Genzel, R., Wright, M. C. H., Jaffe, D. T., Stutzki, J., & Harris, A. I. 1987, *ApJ*, 318, 124
- Haller, J. 1992, Ph.D. Dissertation, University of Arizona, Tucson
- Haller, J. W., Rieke, M. J., Rieke, G. H., Tamblyn, P., Close, L., & Melia, F. 1996, *ApJ*, 456, 194
- Holtzman, J. A. et al. 1993, *AJ*, 106, 1826
- Humphreys, R. M. 1978, *ApJS*, 38, 309

- Jackson, J. M., Geis, N., Genzel, R., Harris, A. I., Madden, S., Poglitsch, A., Stacey, G. J., & Townes, C. H. 1993, *ApJ*, 402, 173
- Johnson, H. 1966, *ARA&A*, 4, 193
- Kent, S. M. 1992, *ApJ*, 387, 181
- Kleinmann, S. G. & Hall, D. N. B. 1986, *ApJS*, 62, 501
- Krabbe, A., Genzel, R., Drapatz, S., & Rotaciuc, V. 1991, *ApJ*, 382, L19
- Krabbe, A. et al. 1995, *ApJ*, 447, L95
- Lambert, D. L., Gustafsson, B., Eriksson, K., & Hinkle, K. H. 1986, *ApJS*, 62, 373
- Lançon, A. & Rocca-Volmerange, B. 1992, *A&AS*, 96, 593
- Lançon, A. & Mouhcine, M. 2002, *A&A*, 393, 167
- Lafon, J.-P. J. & Berruyer, N. 1991, *A&A Rev.*, 2, 249
- Lebofsky, M. J., Rieke, G. H., & Tokunaga, A. T. 1982*a*, *ApJ*, 263, 736
- Lebofsky, M. J., Rieke, G. H., Deshpande, M. R., & Kemp, J. C. 1982*b*, *ApJ*, 263, 672
- Lee, Y. 1992, *AJ*, 104, 1780
- Liszt, H. S. & Burton, W. B. 1980, *ApJ*, 236, 779
- Libonate, S., Pipher, J. L., Forrest, W. J., & Ashby, M. L. N. 1995, *ApJ*, 439, 202
- Lindqvist, M., Habing, H. J., & Winnberg, A. 1992, *A&A*, 259, 118
- Little, S. J. & Price, S. D. 1985, *AJ*, 90, 1812
- Luck, R. E. & Bond, H. E. 1980, *ApJ*, 241, 218
- Luck, R. E. 1982*a*, *ApJ*, 263, 215
- Luck, R. E. 1982*b*, *ApJ*, 256, 177
- Luck, R. E. & Bond, H. E. 1989, *ApJS*, 71, 559
- Massey, P., Johnson, K. E., & Degioia-Eastwood, K. 1995, *ApJ*, 454, 151
- Mathis, J.S. 1990, *ARA&A*, 28, 37

- McGinn, M. T., Sellgren, K., Becklin, E. E., & Hall, D. N. B. 1989, *ApJ*, 338, 824
- McWilliam, A. & Rich, R. M. 1994, *ApJS*, 91, 749
- Mezger, P. G., Zylka, R., Philipp, S., & Launhardt, R. 1999, *A&A*, 348, 457
- Miralda-Escudé, J. & Gould, A. 2000, *ApJ*, 545, 847
- Moneti, A., Glass, I. S., & Moorwood, A. F. M. 1994, *MNRAS*, 268, 194
- Morris, M. 1993, *ApJ*, 408, 496
- Morris, M. & Serabyn, E. 1996, *ARA&A*, 34, 645
- Mulder, W. A. & Liem, B. T. 1986, *A&A*, 157, 148
- Najarro, F., Hillier, D. J., Kudritzki, R. P., Krabbe, A., Genzel, R., Lutz, D., Drapatz, S., & Geballe, T. R. 1994, *A&A*, 285, 573
- Najarro, F., Krabbe, A., Genzel, R., Lutz, D., Kudritzki, R. P., & Hillier, D. J. 1997, *A&A*, 325, 700
- Narayanan, V. K., Gould, A., & DePoy, D. L. 1996, *ApJ*, 472, 183
- Oliva, E. & Origlia, L. 1992, *A&A*, 254, 466
- Olsen, K. A. G. 1999, *AJ*, 117, 2244
- Ott, T., Eckart, A., & Genzel, R. 1999, *ApJ*, 523, 248
- Paczynski, B. 1970, *Acta Astron.*, 20, 47
- Perryman, M. A. C. et al. 1997, *A&A*, 323, L49
- Philipp, S., Zylka, R., Mezger, P. G., Duschl, W. J., Herbst, T., & Tuffs, R. J. 1999, *A&A*, 348, 768
- Pogge, R. W. et al. 1998, *Proc. SPIE*, 3354, 414
- Portegies Zwart, S. F., Makino, J., McMillan, S. L. W., & Hut, P. 2002, *ApJ*, 565, 265
- Ramírez, S. V., DePoy, D. L., Frogel, J. A., Sellgren, K., & Blum, R. D. 1997, *AJ*, 113, 1411
- Ramírez, S. V., Sellgren, K., Carr, J. S., Balachandran, S. C., Blum, R., Terndrup, D. M., & Steed, A. 2000, *ApJ*, 537, 205

- Reid, M. J. 1993, *ARA&A*, 31, 345
- Richichi, A., Ragland, S., Stecklum, B., & Leinert, C. 1998, *A&A*, 338, 527
- Saha, P., Bicknell, G. V., & McGregor, P. J. 1996, *ApJ*, 467, 636
- Salpeter, E. E. 1955, *ApJ*, 121, 161
- Sadler, E. M., Rich, R. M., & Terndrup, D. M. 1996, *AJ*, 112, 171
- Sanders, R. H. 1999, *ASP Conf. Ser. 186: The Central Parsecs of the Galaxy*, 250
- Schödel, R. et al. 2002, *Nature*, 419, 694
- Sellgren, K., Hall, D. N. B., Kleinmann, S. G., & Scoville, N. Z. 1987, *ApJ*, 317, 881
- Sellgren, K., McGinn, M. T., Becklin, E. E., & Hall, D. N. 1990, *ApJ*, 359, 112
- Sjouwerman, L. O., Habing, H. J., Lindqvist, M., van Langevelde, H. J., & Winnberg, A. 1999, *ASP Conf. Ser. 186: The Central Parsecs of the Galaxy*, 379
- Smith, V. V. & Lambert, D. L. 1985, *ApJ*, 294, 326
- Smith, V. V. & Lambert, D. L. 1986, *ApJ*, 311, 843
- Smith, V. V. & Lambert, D. L. 1990, *ApJS*, 72, 387
- Stanek, K. Z., Mateo, M., Udalski, A., Szymanski, M., Kaluzny, J., & Kubiak, M. 1994, *ApJ*, 429, L73
- Strecker, D. W., Erickson, E. F., & Witteborn, F. C. 1978, *AJ*, 83, 26
- Stetson, P. 1987, *PASP*, 99, 191
- Tamblyn, P., Rieke, G. H., Hanson, M. M., Close, L. M., McCarthy, D. W., & Rieke, M. J. 1996, *ApJ*, 456, 206
- Tamura, M., Werner, M. W., Becklin, E. E., & Phinney, E. S. 1996, *ApJ*, 467, 645
- Tanner, A., et al. 2003, *Astron. Nachr.*, Vol. 324, No. S1 (2003), Special Supplement "The central 300 parsecs of the Milky Way", Eds. A. Cotera, H. Falcke, T. R. Geballe, S. Markoff
- Terndrup, D. M. 1988, *AJ*, 96, 884
- Tiede, G. P., Frogel, J. A., & Terndrup, D. M. 1995, *AJ*, 110, 2788

- Tollestrup, E. V., Becklin, E. E., & Capps, R. W. 1989, *AJ*, 98, 204
- van Belle, G. T., Dyck, H. M., Thompson, R. R., Benson, J. A., & Kannappan, S. J. 1997, *AJ*, 114, 2150
- van Leeuwen, F., Feast, M. W., Whitelock, P. A., & Yudin, B. 1997, *MNRAS*, 287, 955
- van Loon, J. et al. 2002, astro-ph/0210073
- Weiland, J. L. et al. 1994, *ApJ*, 425, L81
- Wood, P. R., Habing, H. J., & McGregor, P. J. 1998, *A&A*, 336, 925
- Zoccali, M., Cassisi, S., Frogel, J. A., Gould, A., Ortolani, S., Renzini, A., Rich, R. M., & Stephens, A. W. 2000, *ApJ*, 530, 418

Table 1. Comparison Star Table of Observations

HR	HD	Other	T_{eff} (K)	M_{bol}	SpTyp	T_{eff} Reference ^a	M_{bol} Reference ^a	Obs Date	Instrument ^c
GIANTS									
HR6418	HD156283	π Her	4100	-3.34	K3II	Dy98	Hip+La91	1999 May 05	MOSAIC
HR4299	HD095578	61 Leo	3700	-3.04	M0III	Fe90	Hip+La91	1999 March 03	MOSAIC
...	HD119667	BD -02 3730	3700	-5.10	M1Swk	SL90	SL90	1999 March 01	MOSAIC
HR5154	HD119228	IQ UMa	3600	-3.60	M2III	Fe90	Hip+La91	1999 March 02	MOSAIC
...	HD147923	BD +57 1671	3600	-5.20	M2S	SL90	SL90	1999 May 04	MOSAIC
...	...	BD+062063	3550	-5.70	M3S	SL90	SL90	1999 March 04	MOSAIC
...	HD189581	...	3500	-4.90	M3S4*2	SL90	SL90	1997 July 20	IRS
HR8714	HD216672	HR Peg	3500	-3.30	M3S5,3	SL86	SL86	1997 July 19	IRS
...	HD096360	HL UMa	3550	-5.70	M3Swk	SL90	SL90	1999 March 01	MOSAIC
HR6039	HD145713	LQ Her	3460	-3.08	M4III	Dy98	Hip+La91	1999 May 05	MOSAIC
HR7139	HD175588	δ Lyr	3650	-6.15	M4II	Dy96, Dy98	Hip+La91	1999 May 06	MOSAIC
HR7009	HD172380	XY Lyr	3400	-4.93	M4II:	Dy96, Dy98	Hip+La91	1999 May 04	MOSAIC
...	HD167539	...	3450	-5.60	M4Swk	SL90	SL90	1999 May 05	MOSAIC
HR8818	HD218655	DL Gru	3520	-3.70	M4III	Dy98 T_{eff} v Sp	Hip+La91	1997 July 20	IRS
HR5299	HD123657	BY Boo	3500	-3.10	M4.5III	Dy96, Dy98, SL85	SL85	1999 March 01	MOSAIC
HR5512	HD130144	EK Boo	3610	-4.32	M5III	Dy96, Dy98	Hip+La91	1999 May 06	MOSAIC
HR4909	HD112264	TU CVn	3320	-3.79	M5III	Dy96, Dy98	Hip+La91	1999 May 05	MOSAIC
HR4949	HD113866	FS Com	3420	-3.54	M5III	Dy98	Hip+La91	1999 May 04	MOSAIC
HR6702	HD163990	OP Her	3450	-3.40	M5II-III	Dy96, Dy98, SL85	SL85	1999 May 04	MOSAIC
HR8637	HD214966	19 PsA	3410	-3.50	M5III	Dy98 T_{eff} v Sp	Hip+La91	1997 July 20	IRS
HR0085	HD001760	T Cet	3360	-4.50	M5-6Ib-II	Dy98 T_{eff} v Sp	Be98	2000 July 22	OSIRIS
HR6146	HD148783	g Her	3380	-5.50	M6III	Dy96, Dy98, SL85	SL85	1999 March 03	MOSAIC
HR3639	HD078712	RS Cnc	3190	-5.50	M6IIIas	Dy96, Dy98, SL86	SL86	1999 March 03	MOSAIC
HR1492	HD29712	R Dor	3060	-4.00	M8IIIe	Dy98 T_{eff} v Sp	Dumm98	2000 July 22	OSIRIS
...	HD207076	EP Aqr	3240	-3.80	M8IIIvar	Dy98 T_{eff} v Sp	Dumm98	2000 July 22	OSIRIS
SUPERGIANTS									
HR9103	HD225212	3 Cet	3860	-5.25	K3Iab	Dy98 T_{eff} v Sp	Lu82b, La91	1997 July 19	IRS
HR8726	HD216946	...	3650	-4.90	K5Iab	Dy98 T_{eff} v Sp	EFH85+Hip	BSD96 ^b	...
...	HD163428	...	3800	-6.81	K5II	Lu82a	Hu78+La91	1998 May 18	IRS
...	...	CD-603621	3720	-6.29	M0Ib	Dy98 T_{eff} v Sp	Hu78+La91	1998 May 18	IRS
...	HD316496	KW Sgr	3620	-8.90	MI	Dy98 T_{eff} v Sp	Hu78	1999 July 21	OSIRIS
HR2197	HD042543	BU Gem	3800	-7.88	M1Ia-ab	LB80	Hu78+La91	1999 March 03	MOSAIC

Table 1—Continued

HR	HD	Other	T_{eff} (K)	M_{bol}	SpTyp	T_{eff} Reference ^a	M_{bol} Reference ^a	Obs Date	Instrument ^c
HR2061	HD039801	α Ori	3540	−6.90	M1I	CSB00	Hip+La91	BSD96 ^b	...
HR2190	HD042475	TV Gem	3520	−7.88	M1Iab	Ri98	Hu78+La91	1999 March 03	MOSAIC
...	HD143183	...	3560	−9.00	M1-2I	Dy98 T_{eff} v Sp	Hu78, La91	1999 July 21	OSIRIS
HR 8316	HD206936	μ Cep	3510	−10.30	M2Ia	Dy98 T_{eff} v Sp	Hip+EFH85	BSD96 ^b	...
...	HD14469	SU Per	3350	−7.90	M3.5Ia	Dy98 T_{eff} v Sp	Hip+EFH85	BSD96 ^b	...
...	...	KY Cyg	3310	−9.30	M3.9Iab	Dy98 T_{eff} v Sp	EFH85+MJE95	LVR92 ^b	...
...	HD172804	...	3400	−6.00	M4S5/6-	SL90	SL90	1999 May 06	MOSAIC
...	...	BC Cyg	3300	−9.30	M4Ia	Dy98 T_{eff} v Sp	EFH85+MJE95	LVR92 ^b	...
MIRAS									
HR5894	HD141850	R Ser	2800	−3.63	M7IIIe	Ba98	Hip+BL96	1999 May 06	MOSAIC
HR5080	HD117287	R Hya	2660	−8.30 ^d	M7IIIe	Ba98	vL97	1999 July 21	OSIRIS
HR0681	HD014386	<i>o</i> Cet	2400	−4.80	M7IIIe	Ba98	vL97	2000 July 23	OSIRIS
HR8992	HD222800	R Aqr	2570	−4.10	M7IIIpevar	Ba98	vL97	1999 July 21	OSIRIS

Note. — The choice for inclusion with giants or supergiants for stars with luminosity class II or with no luminosity class (the S-stars) was made based on their measured CO strength; see §3.2.1

^aReferences: Dy98 – Dyck et al. (1998), Fe90 – Fernandez-Villacanas, Rego, & Cornide (1990), SL90 – Smith & Lambert (1990), SL86 – Smith & Lambert (1986), Dy96 – Dyck et al. (1996), Ram97 – Ramirez et al. (1997), SL85 – Smith & Lambert (1985), Lu82a – Luck (1982a), LB80 – Luck & Bond (1980), CSB00 – Carr et al. (2000), Ri98 – Richichi et al. (1998), Ba98 – Barthes (1998), La86 – Lambert et al. (1986), vB97 – van Belle et al. (1997), Hip – Perryman et al. (1997), La91 – Lafon & Berruyer (1991), Be98 – Bedding & Zijlstra (1998), Dumm98 – Dumm & Schild (1998), Lu82b – Luck (1982), Hu78 – Humphreys (1978), EFH85 – Elias, Frogel, & Humphreys (1985), MJE95 – Massey, Johnson, & Degioia-Eastwood (1995), BL96 – Benson & Little-Marenin (1996), vL97 – van Leeuwen et al. (1997)

^bAnalysis uses spectrum for this star presented by Blum et al. (1996b) or Lançon & Rocca-Volmerange (1992).

^cIRS (CTIO 4m): $\lambda/\Delta\lambda = 560$, OSIRIS (CTIO 4m): $\lambda/\Delta\lambda = 1200$, MOSAIC (MDM 1.3m): $\lambda/\Delta\lambda = 750$

^dThe M_{bol} for R Hya is more luminous than the predicted maximum for AGB stars given by Paczyński (1970); see also the discussion by Blum et al. (1996b). However the 1- σ uncertainty on its distance encompasses the luminosity limit.

Table 2. Galactic Center Stars

Name ^a	Number ^b	Offset RA (") ^c	Offset Dec (") ^c	K^d	$J - K^d$	$H - K^d$	Obs Date / Ref	Instrument ^e	Notes
	1	-40.1	-8.0	10.40±0.08	...	2.54±0.11	2000 July 22	OSIRIS	
	2	-38.3	-22.6	10.27±0.05	...	2.51±0.07	2000 July 22	OSIRIS	
	4	-34.4	-18.7	10.36±0.04	6.85±0.07	2.74±0.06	2000 July 22	OSIRIS	
	5	-29.4	-23.2	10.26±0.03	6.61±0.06	2.62±0.05	2000 July 22	OSIRIS	
	6	-28.5	-40.4	9.67±0.03	...	3.02±0.06	1998 May 16	IRS	
	7	-26.9	18.9	9.80±0.03	7.15±0.06	2.76±0.05	1998 May 15	IRS	
	8	-24.0	18.4	10.24±0.06	6.65±0.07	2.51±0.07	1998 May 18	IRS	
	9	-23.0	16.4	9.92±0.04	6.29±0.05	2.42±0.05	1998 May 17	IRS	
	10	-23.0	12.0	10.44±0.04	7.11±0.09	2.99±0.05	2000 July 22	OSIRIS	
	11	-22.4	41.9	9.22±0.14	...	2.28±0.14	1998 May 16	IRS	
	13	-20.1	-32.2	10.06±0.03	7.42±0.07	3.33±0.05	2000 July 22	OSIRIS	
	14	-19.3	25.4	10.48±0.03	6.75±0.05	2.68±0.05	2000 July 22	OSIRIS	
	17	-16.1	18.5	9.74±0.03	6.07±0.04	2.48±0.05	1998 May 16	IRS	
	18	-13.7	15.3	10.18±0.04	...	3.16±0.05	1998 May 17	IRS	
	19	-13.3	-16.9	10.14±0.03	7.57±0.15	3.01±0.05	1998 May 17	IRS	
	23	-9.6	6.5	9.75±0.03	6.14±0.04	2.31±0.05	1998 May 17	IRS	
	27	-9.1	-34.8	9.02±0.03	...	2.66±0.05	1998 May 15	IRS	
IRS 11	28	-8.4	8.0	9.17±0.07	5.95±0.07	1.99±0.08	1998 May 17	IRS	RAM00
IRS 30	35	-6.6	0.2	10.49±0.05	7.11±0.16	2.49±0.11			
IRS 6E	38	-5.53	-5.08	10.06±0.06	...	4.26±0.17	Krabbe et al. (1995)		hot/young star
	40	-4.9	-33.8	10.09±0.05	...	2.69±0.06	1998 May 18	IRS	
	41	-4.5	-30.3	10.14±0.09	...	2.39±0.10	1998 May 17	IRS	
	43	-4.3	-21.8	10.07±0.03	6.13±0.05	2.29±0.05	1998 May 17	IRS	
IRS 2	45	-4.2	-10.2	10.57±0.06	...	3.65±0.13			
IRS 34	46	-4.13	-4.09	10.48±0.08	...	2.83±0.16	Krabbe et al. (1995)		hot/young star
IRS 12S	47	-4.1	-14.6	9.95±0.05	5.85±0.06	2.18±0.06	1998 May 17	IRS	
IRS 22	48	-3.9	-32.0	8.03±0.03	5.13±0.04	1.77±0.05	1997 July 20	IRS	RAM00
IRS 2L	49	-3.9	-9.6	11.68±0.20			
IRS 12N	50	-3.9	-12.9	8.58±0.04	6.95±0.05	2.83±0.06	1997 July 20	IRS	BSD96 LPV
	51	-3.5	-7.2	10.14±0.20	...	3.49±0.20			
IRS 13E	52	-3.37	-7.51	9.82±0.13	5.71±0.14	2.34±0.14	Blum et al. (1995b)		hot/young star
IRS 3	53	-2.45	-2.01	11.16±0.11	...	3.06±0.07	Krabbe et al. (1995)		hot/young star
IRS 29N	56	-1.79	-4.41	9.96±0.11	...	4.36±0.13	Krabbe et al. (1995)		hot/young star
IRS 14SW	60	-0.7	-15.1	10.15±0.04	6.72±0.07	2.59±0.06			
	64	-0.2	31.5	10.13±0.03	6.53±0.05	2.51±0.05	1998 May 18	IRS	
IRS 7	66	0.0	0.0	6.40±0.03	6.64±0.04	2.42±0.10	1997 July 20	IRS	CSB00, RAM00
IRS 14NE	68	0.4	-14.2	9.75±0.04	6.80±0.06	2.64±0.06	1998 May 17	IRS	

Table 2—Continued

Name ^a	Number ^b	Offset RA (″) ^c	Offset Dec (″) ^c	K^d	$J - K^d$	$H - K^d$	Obs Date / Ref	Instrument ^e	Notes
	69	0.4	-34.0	9.79±0.03	7.02±0.08	2.75±0.05	1998 May 16	IRS	
	70	0.4	-28.2	9.88±0.06	6.30±0.07	2.49±0.08	1998 May 16	IRS	
IRS 16SW	71	0.67	-7.15	9.60±0.05	5.15±0.06	2.00±0.07	Krabbe et al. (1995)		young/hot star
F95B	72 ^f	0.8	-36.3	9.05±0.04	3.74±0.05	1.27±0.05	1998 May 15	IRS	RAM00
IRS 15NE	75	1.4	5.6	8.96±0.04	6.03±0.05	2.41±0.05	1997 July 20	IRS	He I emission ^g
MPE 1.6-6.8	77	1.58	-7.21	9.98±0.06	6.00±0.08	2.42±0.08	Krabbe et al. (1995)		young/hot star
IRS 8	78	1.88	23.9	10.49±0.06	...	4.02±0.09	18 May 98	IRS	young/hot star
	79	2.0	42.7	9.73±0.13	6.60±0.13	2.28±0.13	1998 May 16	IRS	
IRS 21	81	2.22	-8.83	10.40±0.05	...	3.95±0.04	Krabbe et al. (1995)		young/hot star
IRS 16NE	83	2.89	-4.90	9.01±0.05	5.00±0.06	1.93±0.06	Tamblyn et al. (1996)		young/hot star
	84	3.1	-17.5	9.88±0.04	7.38±0.08	3.06±0.07	1998 May 15	IRS	
IRS 9	91	5.4	-12.6	8.61±0.03	7.33±0.07	2.24±0.04	1997 July 20	IRS	BSD96 LPV
IRS 1W	92	5.42	-5.61	8.81±0.04	6.21±0.06	3.13±0.07	Blum et al. (1995 ^b)		young/hot star
IRS 1NE	96	7.3	-4.3	10.00±0.07	...	2.50±0.09	BSD96 ^h		K -band only ⁱ
IRS 1SE	97	7.5	-6.6	10.23±0.04	6.66±0.11	2.46±0.06	BSD96 ^h		K -band only ⁱ
IRS10EL	98	8.1	-1.8	10.75±0.09			
	99	8.6	-24.8	9.76±0.03	6.50±0.05	2.45±0.05	1998 May 16	IRS	
IRS 28	102	10.6	-12.1	9.36±0.03	6.94±0.05	2.81±0.05	1998 May 15	IRS	BSD96 LPV
OSU C2	103	10.8	-5.0	10.10±0.04	6.20±0.06	2.35±0.06	1998 May 17	IRS	
	105	13.3	-0.7	8.91±0.03	6.28±0.04	2.32±0.05	1997 July 20	IRS	
	107	13.7	17.5	10.10±0.03	6.27±0.04	2.35±0.04	1998 May 17	IRS	
IRS 19	108	14.4	-25.7	8.22±0.04	6.59±0.04	2.61±0.06	1997 July 20	IRS	RAM00
IRS 18	109	14.9	-17.4	9.50±0.03	6.36±0.04	2.40±0.04	1998 May 16	IRS	
	110	15.6	-28.6	10.07±0.04	7.09±0.07	2.95±0.05	1998 May 17	IRS	
OSUC3	112	18.3	44.6	10.73±0.04	...	3.06±0.05	BSD96 ^h		K -band only ⁱ
	113	17.7	-0.9	10.01±0.04	...	2.59±0.07	1998 May 18	IRS	
	114	18.3	44.6	8.60±0.03	5.74±0.05	2.17±0.05	1997 July 20	IRS	RAM00
	119	23.3	-25.1	10.38±0.03	6.72±0.06	2.59±0.05	2000 July 23	OSIRIS	
	120	23.3	-3.2	10.48±0.03	7.00±0.07	2.75±0.05	2000 July 23	OSIRIS	
	121	23.5	17.3	9.52±0.03	7.13±0.04	2.83±0.04	1998 May 15	IRS	
	123	28.3	3.6	10.04±0.03	6.88±0.05	2.70±0.04	1998 May 17	IRS	
	124	32.5	30.9	9.10±0.03	5.34±0.04	1.96±0.04	1998 May 15	IRS	RAM00
	126	35.3	28	9.69±0.03	6.86±0.05	2.85±0.05	1998 May 15	IRS	
IRS 24	128	36.7	24.2	8.26±0.04	6.36±0.06	2.45±0.05	1997 July 20	IRS	BSD96 LPV
	129	38.8	39.4	9.38±0.03	5.47±0.04	2.11±0.05	1998 May 16	IRS	RAM00
	131	40.0	9.4	8.91±0.03	5.31±0.04	1.90±0.05	1997 July 20	IRS	
	132	40.7	5.5	10.24±0.03	6.23±0.05	2.44±0.05	1998 May 18	IRS	

Table 2—Continued

Name ^a	Number ^b	Offset RA (″) ^c	Offset Dec (″) ^c	K^d	$J - K^d$	$H - K^d$	Obs Date / Ref	Instrument ^e	Notes
OSUC4	133	40.7	-29.7	9.20±0.03	6.54±0.04	2.63±0.04	1998 May 15	IRS	
	135	40.8	-4.5	10.67±0.03	...	2.67±0.04	BSD96 ^h		K -band only ⁱ
IRS 23	136	42.5	8.2	8.62±0.03	6.51±0.04	2.58±0.04	1997 July 20	IRS	BSD96 LPV
	140	46.8	15.8	9.44±0.03	5.73±0.04	2.16±0.04	1998 May 15	IRS	RAM00
	145	62.6	22.0	10.45±0.03	...	3.28±0.05	1998 May 17	IRS	
	146	65.7	11.5	10.45±0.03	7.24±0.09	2.89±0.05	1998 May 18	IRS	
	148	-38.8	9.3	10.52±0.05	...	2.54±0.06	2000 July 23	OSIRIS	
	149	-35.7	-19.1	11.24±0.06	...	3.03±0.08			
	150	-35.6	10.2	10.81±0.05	...	2.78±0.07	2000 July 23	OSIRIS	
	151	-34.6	-23.2	11.22±0.06	...	3.89±0.09	2000 July 23	OSIRIS	
	152	-33.5	16.8	10.83±0.04	...	2.89±0.06			
	153	-32.3	-16.9	11.49±0.06	...	3.41±0.08			
	154	-32.2	-25.5	11.57±0.06	...	3.49±0.09			
	155	-30.3	14.3	10.60±0.04	...	2.77±0.05	2000 July 23	OSIRIS	
	156	-30.2	-17.0	11.65±0.08	...	3.49±0.10			
	158	-29.8	-20.9	11.44±0.04	...	3.37±0.06			
	159	-29.0	-33.2	11.43±0.04	...	3.20±0.06			
	160	-28.3	-47.7	11.16±0.04	...	3.11±0.06			
	162	65.8	45.8	10.84±0.17	2000 July 24	OSIRIS	
	163	-26.3	-10.5	10.67±0.04	6.90±0.08	2.79±0.06			
	164	-25.7	-44.5	11.47±0.04	...	3.43±0.06			
	165	-22.6	35.2	11.06±0.04	7.46±0.20	3.06±0.05			
	166	-19.8	-6.3	11.73±0.03	...	3.37±0.05			
	167	-19.5	29.0	10.85±0.03	...	3.70±0.06	2000 July 23	OSIRIS	
	168	-11.5	40.8	10.70±0.04	7.08±0.09	2.71±0.05	2000 July 24	OSIRIS	
	169	-11.3	-13.9	11.15±0.05	...	3.23±0.10			
	170	-10.2	20.8	10.51±0.05	...	3.25±0.07	2000 July 23	OSIRIS	K -band only ⁱ
	171	-10.2	-42.8	12.14±0.04	...	3.73±0.07			
	172	-10.0	-6.3	11.09±0.04	...	3.14±0.07			
	173	-9.7	-37.1	10.95±0.04	...	3.79±0.08	2000 July 23	OSIRIS	K -band only ⁱ
	174	-7.9	8.0	10.81±0.26	...	4.24±0.26			
	175	-6.5	-15.8	10.96±0.06	...	2.77±0.07			
	176	-5.0	36.3	10.67±0.04	...	2.82±0.05	2000 July 24	OSIRIS	
	177	-4.6	-30.1	10.90±0.17			
	178	-4.5	-30.3	10.14±0.09	...	2.39±0.10			
	180	-2.8	-49.6	10.76±0.04	...	4.10±0.06	2000 July 23	OSIRIS	
	181	1.6	-21.2	11.30±0.04	...	3.39±0.11			

Table 2—Continued

Name ^a	Number ^b	Offset RA (″) ^c	Offset Dec (″) ^c	K^d	$J - K^d$	$H - K^d$	Obs Date / Ref	Instrument ^e	Notes
	182	2.6	35.3	10.52±0.04	7.19±0.08	2.84±0.06	2000 July 22	OSIRIS	
	185	5.0	-16.2	11.30±0.05	...	3.31±0.16			
	186	6.0	8.8	10.94±0.04	...	3.25±0.10	2000 July 24	OSIRIS	
	188	7.5	-38.1	12.40±0.04	...	3.76±0.10			
	189	11.1	-15.3	11.03±0.03	7.38±0.15	3.09±0.05			
	190	13.5	-28.4	11.20±0.04	...	3.25±0.07			
	191	14.6	-27.5	11.66±0.06	...	4.51±0.30			
	192	22.6	-44.8	12.75±0.05	...	4.03±0.23			
	194	25.4	-49.7	12.75±0.04	...	4.29±0.19			
	195	26.3	-2.9	10.75±0.04	...	3.01±0.06			
	197	26.9	1.5	10.59±0.03	6.95±0.06	2.91±0.05	2000 July 24	OSIRIS	
	198	27.3	-24.8	10.76±0.03	7.07±0.08	2.89±0.04	2000 July 24	OSIRIS	
	199	30.3	-38.8	12.21±0.03	...	3.95±0.08			
	201	37.8	3.7	12.01±0.04	...	3.52±0.09			
	202	37.9	-42.9	12.28±0.04	...	3.74±0.07			
	203	38.8	46.6	10.73±0.08			
	204	40.4	-47.8	11.51±0.04	...	3.80±0.06			
	205	40.7	2.7	10.82±0.03	...	2.90±0.05			
	206	41.3	-6.2	11.92±0.04	...	4.30±0.15			
	208	47.5	-37.7	11.91±0.03	...	4.12±0.07			
	209	54.2	-24.1	12.98±0.04	...	4.15±0.24			
	210	54.7	7.3	11.43±0.03	...	3.71±0.06			
	211	57.8	-36.8	10.54±0.03	7.09±0.07	2.95±0.04	2000 July 22	OSIRIS	
	212	59.7	15.0	11.51±0.04	...	3.48±0.09			
	213	62.4	-34.6	11.51±0.04	...	3.63±0.06			
	214	63.3	12.4	10.61±0.04	...	4.06±0.08	2000 July 23	OSIRIS	K -band only ⁱ
VR5-7 ^j				7.30±0.15	...	2.30±0.18	1998 May 18	IRS	RAM00

Table 2—Continued

Name ^a	Number ^b	Offset RA (″) ^c	Offset Dec (″) ^c	K^d	$J - K^d$	$H - K^d$	Obs Date / Ref	Instrument ^e	Notes
-------------------	---------------------	----------------------------	-----------------------------	-------	-----------	-----------	----------------	-------------------------	-------

Note. — Objects indicated with CSB00 or RAM00 have been observed at high spectral resolution by Carr et al. (2000) and Ramírez et al. (2000), respectively. Long period variable (LPV) candidates are given by Blum et al. (1996b, BSD96). Stars indicated as “hot/young” are previously identified massive young stars which lie in the K_o selected sample of this paper; see text.

^aObject names are as given by Becklin & Neugebauer (1975), Lebofsky et al. (1982b), Tollestrup, Becklin, & Capps (1989), Krabbe et al. (1995), and Blum et al. (1996a)

^bNumber corresponds to sequence in Blum et al. (1996a). Data tables in Blum et al. (1996a) were truncated at # 147.

^cOffset is from IRS 7: α (2000) = 17h45m40s, δ (2000) = $-29^\circ 00' 22.7''$; see Blum et al. (1996a).

^d K magnitude, $J - K$, and $H - K$ taken from Blum et al. (1996a). For #'s 1, 2, 6, 11, 40, 51, 53, 78, 81, 148, 162, 170, 174, 175, and 183 photometry was derived using new unpublished J and/or H images which were not available to Blum et al. (1996a). These new data were obtained with OSIRIS on 1999 March 03, but the field of view did not completely cover the same field as for BDS96, thus some stars without H magnitudes given by BDS96 were not observed. Improved H magnitudes could not be extracted for several stars which were in the BDS96 field of view, primarily due to crowding.

^eIRS (CTIO 4m): $\lambda/\Delta\lambda = 560$, OSIRIS (CTIO 4m): $\lambda/\Delta\lambda = 1200$, MOSAIC (MDM 1.3m): $\lambda/\Delta\lambda = 750$.

^fStar 72 is included because it was observed and analyzed at high spectral resolution by Ramírez et al. (2000). This star was not used in the star formation history calculation because its K_o is below the cut-off adopted; see §3.3.

^gThe spectrum of IRS 15NE shows strong characteristic cool star features (see Table 6), but also broad He I and Br γ emission suggesting it is a close blend. Because the cool star features are quite strong and the emission-line stars are generally fainter at K than the brighter M stars in the GC, we assume the hot star contribution to this object is not sufficient to remove it from our brightness selected sample.

^hSpectrum taken from Blum et al. (1996b, BSD96).

ⁱAnalysis based on K -band spectrum only; see text, §2.3.

^jThis star is located in the Quintuplet cluster (Moneti, Glass, & Moorwood 1994) and is included for reference. Photometry is taken from Moneti et al. (1994).

Table 3. Comparison Star Indices

HR	HD	Other	SpTyp	T_{eff}	CO (%) ^a	H ₂ O (%) ^a
GIANTS						
HR6418	HD156283	π -Her	K3II	4100	13 \pm 0.7	1 \pm 3
HR4299	HD095578	61-Leo	M0III	3700	15 \pm 0.4	2 \pm 3
...	HD119667	BD-023726	M1Swk	3700	17 \pm 0.5	1 \pm 3
HR5154	HD119228	IQ-UMa	M2III	3600	16 \pm 0.5	-1 \pm 3
...	HD147923	BD+571671	M2S	3600	17 \pm 0.5	0 \pm 3
...	...	BD+062063	M3S	3550	15 \pm 0.5	0 \pm 3
...	HD189581	...	M3S4*2	3500	16 \pm 0.5	3 \pm 3
HR8714	HD216672	HR Peg	M3S5,3	3500	20 \pm 0.5	-2 \pm 3
...	HD096360	HL UMa	M3Swk	3550	16 \pm 0.6	2 \pm 3
HR6039	HD145713	LQ Her	M4III	3460	17 \pm 0.6	0 \pm 3
HR7139	HD175588	δ Lyr	M4II	3650	15 \pm 0.8	-4 \pm 3
HR7009	HD172380	XY Lyr	M4II:	3400	19 \pm 0.5	-2 \pm 3
...	HD167539	...	M4Swk	3450	17 \pm 0.6	1 \pm 3
HR8818	HD218655	DL Gru	M4III	3520	16 \pm 0.7	-1 \pm 3
HR5299	HD123657	BY Boo	M4.5III	3500	18 \pm 0.7	0 \pm 3
HR5512	HD130144	EK Boo	M5III	3610	17 \pm 0.6	-4 \pm 3
HR4909	HD112264	TU CVn	M5III	3320	18 \pm 0.6	4 \pm 3
HR4949	HD113866	FS Com	M5III	3420	17 \pm 0.4	-7 \pm 3
HR6702	HD163990	OP Her	M5II-III	3450	20 \pm 0.5	-1 \pm 3
HR8637	HD214966	19 PsA	M5III	3410	16 \pm 0.7	-3 \pm 3
HR0085	HD001760	T Cet	M5-6Ib-II	3360	20 \pm 1.1	-9 \pm 3
HR6146	HD148783	g Her	M6III	3380	17 \pm 0.7	1 \pm 3
HR3639	HD078712	RS Cnc	M6IIas	3190	19 \pm 0.5	5 \pm 3
HR1492	HD29712	R Dor	M8IIIe	3060	22 \pm 1.4	... ^b
...	HD207076	EP Aqr	M8IIIvar	3240	19 \pm 1.4	... ^b
SUPERGIANTS						
HR9103	HD225212	3 Cet	K3Iab	3860	19 \pm 0.6	1 \pm 3
HR8726	HD216946	...	K5Iab	3650	20 \pm 0.5	2 \pm 3 ^c
...	HD163428	...	K5II	3800	19 \pm 0.5	0 \pm 3
...	...	CD-603621	M0Ib	3720	22 \pm 0.6	-3 \pm 3
...	HD316496	KW Sgr	M1	3620	23 \pm 1.4	-2 \pm 3
HR2197	HD042543	BU Gem	M1Ia-ab	3800	22 \pm 0.6	1 \pm 3
HR2061	HD039801	α Ori	M1I	3540	23 \pm 0.5	2 \pm 3 ^c
HR2190	HD042475	TV Gem	M1Iab	3520	23 \pm 0.7	1 \pm 3
...	HD143183	...	M1-2I	3570	24 \pm 1.4	-3 \pm 3
HR 8316	HD206936	μ Cep	M2Ia	3510	25 \pm 0.5	4 \pm 3 ^c
...	HD14469	SU Per	M3.5Ia	3350	26 \pm 0.5	6 \pm 3 ^c
...	...	KY Cyg	M3.9Iab	3310	25 \pm 1.7	8 \pm 3
...	HD172804	...	M4S5/6-	3400	26 \pm 0.7	1 \pm 3
...	...	BC Cyg	M4Ia	3300	25 \pm 1.7	-2 \pm 3
MIRAS						
HR5894	HD141850	R Ser	M7IIIe	2800	21 \pm 0.6	15 \pm 3
HR5080	HD117287	R Hya	M7IIIe	2660	25 \pm 1.1	43 \pm 3

Table 3—Continued

HR	HD	Other	SpType	T_{eff}	CO (%) ^a	H ₂ O (%) ^a
HR0681	HD014386	<i>o</i> Cet	M7I Ie	2400	16 ± 1.7	37 ± 3
HR8992	HD222800	R Aqr	M7IIIpevar	2570	23 ± 1.2	34 ± 3

^aIndices are % absorption defined as $100 \times (1 - Flux/Cont)$ where *Flux* and *Cont* are the integrated fluxes in 0.015 μm bands in the spectra. For CO, the *Flux* band is centered at 2.302 μm , and the *Cont* band is taken at 2.284 μm . For H₂O, *Flux* is for a band centered at 2.0675 μm , and *Cont* is the same but derived from a fit to the spectral continuum; see text. The uncertainty in the measured H₂O strength is taken from the scatter in the measurements of IIIs and Is; see text.

^bContinuum may have been affected by data taking procedure; see text. Strong expected H₂O absorption not evident.

^c*K*-band spectrum only, continuum fit made in the same way as for stars with *H* and *K*, but only fit in the region between 2.20 and 2.29 μm .

Table 4. Galactic Center Stars Younger than 10 Myr^a

Name ^b	Number ^c	$T_{\text{eff}}/ \text{SpType}^{\text{d}}$	K_{\circ}^{e}	A_K^{e}	M_K^{f}	$M_{\text{bol}}^{\text{d}}$
IRS 6E	38	WC9	3.77 ± 0.28	6.28 ± 0.28	-10.75	
IRS 34	46	WC9	6.47 ± 0.12	4.01 ± 0.22	-8.05	
IRS 13E	52	29000	6.85 ± 0.18	2.97 ± 0.12	-7.67	-11.1
IRS 3	53	featureless	6.78 ± 0.12	4.38 ± 0.11	-7.74	
IRS 29N	56	WC9	3.56 ± 0.25	6.40 ± 0.10	-10.96	
IRS 7	66	3430 ± 240	2.92 ± 0.16	3.48 ± 0.09	-11.60	-9.0
IRS 16SW	71	24000	7.00 ± 0.08	2.60 ± 0.06	-7.52	-11.3
MPE 1.6-6.8	77	WC9	6.65 ± 0.11	3.28 ± 0.08	-7.87	
IRS 8	78	featureless	4.59 ± 0.15	5.90 ± 0.14	-9.93	
IRS 21	81	featureless	4.61 ± 0.08	5.79 ± 0.06	-9.91	
IRS 16NE	83	24000	6.55 ± 0.06	2.45 ± 0.05	-7.97	-11.0
IRS 1W	92	featureless	6.29 ± 0.07	2.42 ± 0.06	-8.23	
VR5-7	...	3570 ± 150	4.13 ± 0.30	3.17 ± 0.28	-10.22	-7.6

^aOnly stars with $K_{\circ} \leq 7.0$ from the list of Blum et al. (1996b) are included in this table.

^bObject names are as given by Becklin & Neugebauer (1975), Lebofsky et al. (1982b), Tollestrup, Becklin, & Capps (1989), Krabbe et al. (1995) and Blum et al. (1996a)

^cNumber corresponds to sequence in Blum et al. (1996a). Data tables in Blum et al. (1996a) were truncated at # 147.

^d $T_{\text{eff}}/ M_{\text{bol}}$ for hot stars IRS 16NE, 16SW, and 13E from Najarro et al. (1997). $T_{\text{eff}}/ M_{\text{bol}}$ for IRS 7 and VR5-7 from present work. Spectral types (SpType) from reference listed in Table 2.

^e K_{\circ} ($= K - A_K$) and A_K taken from Blum et al. (1996a). Stars # 53, 78, and 81 use new unpublished *H*-band magnitudes which were unavailable to Blum et al. (1996a). K_{\circ} and A_K for VR5-7 derived using photometry in Table 2.

^f M_K is derived from K_{\circ} (see Blum et al. 1996a) and a distance modulus of 14.52 (8 kpc, Reid 1993).

Table 5. Completeness and Characteristics of the GC Sample

K_o^a	Percent Complete ^b	Number Observed	Number in K_o LF
$K_o < 4.0$	100%	3	3
$4.0 < K_o < 4.5$	100%	0	0
$4.5 < K_o < 5.0$	100%	7	7
$5.0 < K_o < 5.5$	50%	5	10
$5.5 < K_o < 6.0$	85%	17	20
$6.0 < K_o < 6.5$	78%	18	23
$6.5 < K_o < 7.0$	55%	40	73
Total (cool + hot/young)		90	136
Stars by type:			
Number of GC I			15 ^c
Number of GC III			43
Number of GC LPV			20
Stars Younger than 10 Myr			12 ^c
Stars not Observed			46
Total			136

^aThe original sample is selected from the complete list of stars with $K_o < 7.0$ mag in the central few pc of the Galaxy presented by Blum et al. (1996a).

^bPercentage of stars observed spectroscopically from the list of Blum et al. (1996a) which includes known emission-line stars or featureless young stars; see text and Tables 2 and 4.

^cIRS 7, M I, is counted among the young stars. VR5-7 of the Quintuplet cluster is not counted in this table, nor is #72 which is listed in Table 2 and 6.

Table 6. Galactic Center Star Properties

Name	Number	CO (%)	H ₂ O (%)	Luminosity Class ^b	T_{eff}^c	K_o^d	M_K^e	A_K^d	BC_K^f	ΔA_K^g	M_{bol}^h
	1	21 ± 0.6	−2	I	3710 ± 130	6.85 ± 0.12	−7.67	3.55 ± 0.09	2.6	0.0	−5.07 ± 0.42
	2	20 ± 0.8	17	LPV?	2740 ± 200	6.76 ± 0.12	−7.76	3.51 ± 0.11	3.2	0.5	−4.06 ± 0.42
	4	26 ± 0.9	16	LPV?	2750 ± 200	6.70 ± 0.10	−7.82	3.67 ± 0.06	3.2	0.5	−4.12 ± 0.41
	5	24 ± 0.9	10	III	2930 ± 150	6.74 ± 0.06	−7.78	3.51 ± 0.05	3.2	0.4	−4.18 ± 0.40
	6	17 ± 2.1	32	LPV?	2610 ± 200	5.36 ± 0.11	−9.16	4.31 ± 0.11	3.2	0.5	−5.46 ± 0.41
	7	23 ± 1.9	15	III	3040 ± 250	5.97 ± 0.06	−8.55	3.83 ± 0.05	3.1	0.3	−5.15 ± 0.40
	8	22 ± 1.2	21	LPV?	2710 ± 200	6.73 ± 0.08	−7.79	3.50 ± 0.06	3.2	0.5	−4.09 ± 0.41
	9	20 ± 0.9	10	III	3280 ± 150	6.63 ± 0.06	−7.89	3.29 ± 0.05	2.9	0.2	−4.79 ± 0.40
	10	23 ± 0.9	12	III	3050 ± 150	6.97 ± 0.10	−7.55	3.47 ± 0.10	3.1	0.3	−4.15 ± 0.41
	11	21 ± 1.2	12	III	3190 ± 180	6.08 ± 0.17	−8.44	3.14 ± 0.09	3.0	0.2	−5.24 ± 0.43
	13	23 ± 1.0	17	LPV	2740 ± 200	6.62 ± 0.08	−7.90	3.44 ± 0.07	3.2	0.5	−4.20 ± 0.41
	14	24 ± 0.9	5	I	3470 ± 150	6.88 ± 0.06	−7.64	3.60 ± 0.05	2.6	0.0	−5.04 ± 0.40
	17	21 ± 1.3	7	III	3200 ± 190	6.55 ± 0.06	−7.97	3.20 ± 0.05	3.0	0.2	−4.77 ± 0.40
	18	23 ± 0.7	19	LPV?	2740 ± 200	5.83 ± 0.09	−8.69	4.36 ± 0.09	3.2	0.5	−4.99 ± 0.41
	19	21 ± 1.1	38	LPV?	2560 ± 200	6.03 ± 0.09	−8.49	4.11 ± 0.09	3.2	0.5	−4.79 ± 0.41
	23	21 ± 0.7	8	III	3240 ± 140	6.56 ± 0.05	−7.96	3.18 ± 0.04	3.0	0.2	−4.76 ± 0.40
	27	20 ± 1.5	18	LPV?	2740 ± 200	5.49 ± 0.09	−9.03	3.53 ± 0.09	3.2	0.5	−5.33 ± 0.41
IRS 11	28	22 ± 1.6	9	III	3130 ± 220	6.18 ± 0.09	−8.34	3.00 ± 0.06	3.0	0.3	−5.04 ± 0.41
	40	22 ± 2.0	21	LPV?	2700 ± 200	5.83 ± 0.11	−8.69	4.20 ± 0.10	3.2	0.5	−4.99 ± 0.41
	41	15 ± 1.7	5	III	3680 ± 230	6.92 ± 0.19	−7.60	3.22 ± 0.16	2.7	0.0	−4.90 ± 0.44
	43	17 ± 1.9	7	III	3540 ± 260	6.89 ± 0.06	−7.63	3.18 ± 0.05	2.8	0.0	−4.83 ± 0.40
IRS 12S	47	15 ± 1.1	4	III	3630 ± 170	6.95 ± 0.07	−7.57	3.00 ± 0.06	2.7	0.0	−4.87 ± 0.41
IRS 22	48	21 ± 0.7	4	I	3710 ± 140	5.43 ± 0.14	−9.09	2.52 ± 0.13	2.6	0.0	−6.49 ± 0.42
IRS 12N	50	20 ± 2.1	30	LPV	2630 ± 200	4.74 ± 0.14	−9.78	3.79 ± 0.14	3.2	0.5	−6.08 ± 0.42
	64	23 ± 2.1	17	LPV?	2740 ± 200	6.69 ± 0.05	−7.83	3.44 ± 0.05	3.2	0.5	−4.13 ± 0.40
IRS 7	66	25 ± 1.8	3	I	3430 ± 240	2.92 ± 0.16	−11.60	3.48 ± 0.09	2.6	0.0	−9.00 ± 0.43
IRS14NE	68	23 ± 1.3	17	LPV?	2740 ± 200	6.13 ± 0.07	−8.39	3.61 ± 0.05	3.2	0.5	−4.69 ± 0.41
	69	20 ± 1.7	14	III	3290 ± 230	6.03 ± 0.07	−8.49	3.76 ± 0.06	2.9	0.2	−5.39 ± 0.41
	70	22 ± 1.2	8	III	3160 ± 180	6.57 ± 0.09	−7.95	3.32 ± 0.07	3.0	0.3	−4.65 ± 0.41
F95B	72 ⁱ	17 ± 0.6	4	III	3960 ± 130	7.38 ± 0.06	−7.14	1.67 ± 0.04	2.6	0.0	−4.54 ± 0.40
IRS15NE	75	17 ± 1.1	18	LPV?	2730 ± 200	5.80 ± 0.06	−8.72	3.16 ± 0.05	3.2	0.5	−5.02 ± 0.40
	79	21 ± 0.9	−1	I	3740 ± 150	6.32 ± 0.17	−8.20	3.41 ± 0.11	2.6	0.0	−5.60 ± 0.43
	84	23 ± 1.4	10	III	3050 ± 200	5.85 ± 0.08	−8.67	4.03 ± 0.07	3.1	0.3	−5.27 ± 0.41
IRS 9	91	18 ± 0.9	37	LPV	2570 ± 200	5.21 ± 0.06	−9.31	3.36 ± 0.06	3.2	0.5	−5.61 ± 0.40
IRS 1NE	96	21 ± 2.1	14	III	3220 ± 270	6.52 ± 0.16	−8.00	3.48 ± 0.14	3.0	0.2	−4.80 ± 0.43
IRS 1SE	97	21 ± 1.6	14	III	3220 ± 220	6.78 ± 0.08	−7.74	3.47 ± 0.07	3.0	0.2	−4.54 ± 0.41
	99	22 ± 0.7	7	III	3160 ± 170	6.35 ± 0.05	−8.17	3.41 ± 0.04	3.0	0.3	−4.87 ± 0.40

Table 6—Continued

Name	Number	CO (%)	H ₂ O (%)	Luminosity Class ^b	T_{eff}^c	K_o^d	M_K^e	A_K^d	BC _K ^f	ΔA_K^g	M_{bol}^h
IRS 28	102	20 ± 1.6	19	LPV	2730 ± 200	5.62 ± 0.06	-8.90	3.74 ± 0.05	3.2	0.5	-5.20 ± 0.40
OSU C2	103	23 ± 1.0	11	III	3040 ± 160	6.88 ± 0.07	-7.64	3.22 ± 0.06	3.1	0.3	-4.24 ± 0.41
	105	22 ± 0.6	17	LPV?	2740 ± 200	5.65 ± 0.05	-8.87	3.26 ± 0.04	3.2	0.5	-5.17 ± 0.40
	107	19 ± 1.2	5	III	3330 ± 180	6.84 ± 0.05	-7.68	3.26 ± 0.04	2.9	0.2	-4.58 ± 0.40
IRS 19	108	18 ± 1.7	4	I	3910 ± 230	4.64 ± 0.11	-9.88	3.50 ± 0.10	2.6	0.0	-7.28 ± 0.41
IRS 18	109	20 ± 1.6	4	I	3760 ± 220	6.18 ± 0.05	-8.34	3.32 ± 0.04	2.6	0.0	-5.74 ± 0.40
	110	21 ± 0.9	15	III	3200 ± 150	6.22 ± 0.07	-8.30	3.85 ± 0.05	3.2	0.5	-4.60 ± 0.41
OSUC3	112	24 ± 2.0	12	III	2980 ± 270	6.48 ± 0.06	-8.04	4.25 ± 0.04	3.1	0.4	-4.54 ± 0.40
	113	20 ± 1.0	7	III	3310 ± 160	6.50 ± 0.12	-8.02	3.51 ± 0.11	2.9	0.2	-4.92 ± 0.42
	114	24 ± 1.1	12	III	2970 ± 170	5.65 ± 0.06	-8.87	2.95 ± 0.04	3.2	0.4	-5.27 ± 0.40
	119	22 ± 1.1	7	III	3140 ± 170	6.83 ± 0.06	-7.69	3.56 ± 0.05	3.0	0.3	-4.39 ± 0.40
	120	23 ± 1.0	12	III	3080 ± 160	6.73 ± 0.06	-7.79	3.75 ± 0.06	3.1	0.3	-4.39 ± 0.40
	121	24 ± 1.1	14	III	3000 ± 170	5.68 ± 0.05	-8.84	3.83 ± 0.04	3.1	0.4	-5.34 ± 0.40
	123	21 ± 1.1	8	III	3170 ± 170	6.37 ± 0.05	-8.15	3.67 ± 0.04	3.0	0.3	-4.85 ± 0.40
	124	21 ± 1.2	3	I	3720 ± 180	6.42 ± 0.05	-8.10	2.68 ± 0.04	2.6	0.0	-5.50 ± 0.40
	126	22 ± 1.0	9	III	3110 ± 160	5.99 ± 0.06	-8.53	3.70 ± 0.05	3.1	0.3	-5.13 ± 0.40
IRS 24	128	22 ± 2.6	26	LPV	2660 ± 200	4.92 ± 0.09	-9.60	3.34 ± 0.07	3.2	0.5	-5.90 ± 0.41
	129	20 ± 0.7	2	I	3750 ± 130	6.59 ± 0.06	-7.93	2.79 ± 0.05	2.6	0.0	-5.33 ± 0.40
	131	22 ± 0.9	15	III	3090 ± 150	6.26 ± 0.05	-8.26	2.65 ± 0.04	3.1	0.3	-4.86 ± 0.40
	132	23 ± 0.8	11	III	3050 ± 140	6.98 ± 0.05	-7.54	3.27 ± 0.04	3.1	0.3	-4.14 ± 0.40
	133	19 ± 1.1	14	III	3340 ± 170	5.72 ± 0.05	-8.80	3.48 ± 0.04	2.9	0.2	-5.70 ± 0.40
OSUC4	135	24 ± 1.9	15	III	2940 ± 260	7.00 ± 0.08	-7.52	3.67 ± 0.07	3.2	0.4	-3.92 ± 0.41
IRS 23	136	18 ± 2.1	35	LPV?	2580 ± 200	5.18 ± 0.14	-9.34	3.44 ± 0.13	3.2	0.5	-5.64 ± 0.42
	140	23 ± 0.5	12	III	3050 ± 120	6.50 ± 0.05	-8.02	2.93 ± 0.04	3.1	0.3	-4.62 ± 0.40
	145	18 ± 1.3	23	LPV?	2690 ± 200	5.91 ± 0.09	-8.61	4.54 ± 0.09	3.2	0.5	-4.91 ± 0.41
	146	19 ± 2.2	13	III	3330 ± 290	6.54 ± 0.07	-7.98	3.91 ± 0.06	2.9	0.2	-4.88 ± 0.41
	148	21 ± 1.0	7	III	3170 ± 160	6.97 ± 0.05	-7.55	3.55 ± 0.09	3.0	0.3	-4.25 ± 0.40
	150	22 ± 1.9	8	III	3130 ± 250	6.97 ± 0.12	-7.55	3.84 ± 0.11	3.0	0.3	-4.25 ± 0.42
	151	25 ± 0.9	3	I	3400 ± 150	5.73 ± 0.16	-8.79	3.30 ± 0.15	2.6	0.0	-6.19 ± 0.43
	155	24 ± 1.5	11	III	2930 ± 210	6.79 ± 0.09	-7.73	3.82 ± 0.08	3.2	0.4	-4.13 ± 0.41
	162	26 ± 0.8	3	I	3360 ± 150	5.92 ± 0.17	-8.60	4.93 ± 0.00	2.6	0.0	-6.00 ± 0.43
	167	17 ± 2.8	31	LPV?	2620 ± 200	5.66 ± 0.10	-8.86	5.19 ± 0.09	3.2	0.5	-5.16 ± 0.41
	168	25 ± 0.9	7	I	3430 ± 150	6.92 ± 0.07	-7.60	3.77 ± 0.06	2.6	0.0	-5.00 ± 0.41
	170	22 ± 1.0	5	I	3660 ± 160	5.83 ± 0.12	-8.69	4.68 ± 0.11	2.6	0.0	-6.09 ± 0.42
	173	21 ± 1.0	2	I	3740 ± 160	5.62 ± 0.14	-8.90	5.33 ± 0.13	2.6	0.0	-6.30 ± 0.42
	176	25 ± 0.9	12	III	2880 ± 150	6.79 ± 0.09	-7.73	3.88 ± 0.08	3.2	0.4	-4.13 ± 0.41
	180	25 ± 1.0	14	III	2910 ± 160	4.99 ± 0.10	-9.53	5.77 ± 0.10	3.2	0.4	-5.93 ± 0.41

Table 6—Continued

Name	Number	CO (%)	H ₂ O (%)	Luminosity Class ^b	T_{eff}^c	K_{o}^d	M_K^e	A_K^d	BC_K^f	ΔA_K^g	M_{bol}^h
	182	21 ± 1.0	10	III	3180 ± 160	6.65 ± 0.07	-7.87	3.87 ± 0.06	3.0	0.2	-4.67 ± 0.41
	186	24 ± 1.6	-3	I	3500 ± 220	6.40 ± 0.16	-8.12	4.54 ± 0.15	2.6	0.0	-5.52 ± 0.43
	197	21 ± 1.4	1	I	3680 ± 200	6.82 ± 0.06	-7.70	3.77 ± 0.05	2.6	0.0	-5.10 ± 0.40
	198	25 ± 1.3	10	III	2860 ± 190	6.93 ± 0.06	-7.59	3.82 ± 0.06	3.2	0.4	-3.99 ± 0.40
	211	25 ± 1.1	14	III	2930 ± 170	6.70 ± 0.06	-7.82	3.85 ± 0.05	3.2	0.4	-4.22 ± 0.40
	214	23 ± 1.0	11	III	3080 ± 160	4.91 ± 0.13	-9.61	5.69 ± 0.12	3.1	0.3	-6.21 ± 0.42
VR5-7	...	23 ± 0.9	6	I	3570 ± 150	... ± ...	-10.22	3.10 ± ...	2.6	0.0	-7.62 ± 0.40

^aIndices are % absorption defined as $100 \times (1 - Flux/Cont)$ where $Flux$ and $Cont$ are the integrated fluxes in 0.015 μm bands in the spectra. For CO, the $Flux$ band is centered at 2.302 μm , and the $Cont$ band is taken at 2.284 μm . For H₂O, $Flux$ is for a band centered at 2.0675 μm , and $Cont$ is the same but derived from a fit to the spectral continuum; see text. The uncertainty in the measured H₂O strength (3%) is taken from the scatter in the measurements for comparison star IIIs and Is; see text.

^bThe luminosity class is set by the CO index and the H₂O index; see text.

^c T_{eff} is derived from the CO index using the relationship of CO vs T_{eff} derived for the comparison stars. See the discussion in the text and Figure 2.

^d K_{o} ($= K - A_K$) and A_K taken from Blum et al. (1996a). For #'s 1, 2, 6, 11, 40, 148, 162, and 170 A_K were derived in the same way, but using new unpublished H magnitudes as given in Table 2.

^e M_K is derived from K_{o} and a distance modulus of 14.52 (8 kpc, Reid 1993).

^fBolometric correction to the K_{o} magnitudes. The correction is a linear function of T_{eff} for giants, and a constant for LPV's and supergiants; see text and Blum et al. (1996b).

^gCorrection to A_K to account for the range of intrinsic color in the GC stars. $\Delta A_K = A_K(\text{Blum et al. 1996a}) - A_K(\text{Corrected})$. See text.

^h $M_{\text{bol}} = K_{\text{o}} + BC_K + \Delta A_K - DM$, where DM is the distance modulus to the GC (14.52) for 8 kpc (Reid 1993).

ⁱStar 72 is included because it was observed and analyzed at high spectral resolution by Ramírez et al. (2000). This star was not used in the star formation history calculation because its K_{o} is below the cut-off adopted; see §3.3.

Table 7. Summary of Models Fitted

Model	χ^2_λ	P_λ (%)	M_T ($10^6 M_\odot$)	σ_{M_T}	Age (Gyr)	[Fe/H]	SFR ($10^{-4} M_\odot \text{ yr}^{-1}$)	σ_{SFR}
Model A	231.9	58.9	9.9	3.0	0.01 – 0.10	0.0	33.3	9.7
					0.10 – 1.00	0.0	2.9	1.9
					1.00 – 5.00	0.0	4.5	1.6
					5.00 – 12.00	0.0	10.8	4.1
Model A, IMF slope varied	232.4	54.8	16.4	4.3	0.01 – 0.10	0.0	28.3	8.5
					0.10 – 1.00	0.0	3.4	2.4
					1.00 – 5.00	0.0	7.3	2.4
					5.00 – 12.00	0.0	18.4	7.3
Model B	233.3	13.7	16.1	4.1	0.01 – 0.10	0.0	30.2	9.7
					0.10 – 1.00	0.0	3.8	1.8
					1.00 – 5.00	0.0	0.00	1.8
					5.00 – 12.00	-0.2	22.1	5.7
Model 1	238.1	11.0	9.07	2.4	0.01 – 0.50	0.0	10.7	2.4
					0.50 – 3.00	0.0	3.1	1.3
					3.00 – 12.00	0.0	8.7	2.7
Model 2	238.5	2.2	12.1	1.8	0.01 – 0.50	0.0	12.3	2.4
					0.50 – 3.00	0.0	0.00	0.10
					3.00 – 12.00	-0.2	12.8	2.0

[Figure 1 about here.]

[Figure 2 about here.]

[Figure 3 about here.]

[Figure 4 about here.]

[Figure 5 about here.]

[Figure 6 about here.]

[Figure 7 about here.]

[Figure 8 about here.]

[Figure 9 about here.]

[Figure 10 about here.]

[Figure 11 about here.]

[Figure 12 about here.]

[Figure 13 about here.]

[Figure 14 about here.]

[Figure 15 about here.]

[Figure 16 about here.]

[Figure 17 about here.]

[Figure 18 about here.]

[Figure 19 about here.]

[Figure 20 about here.]

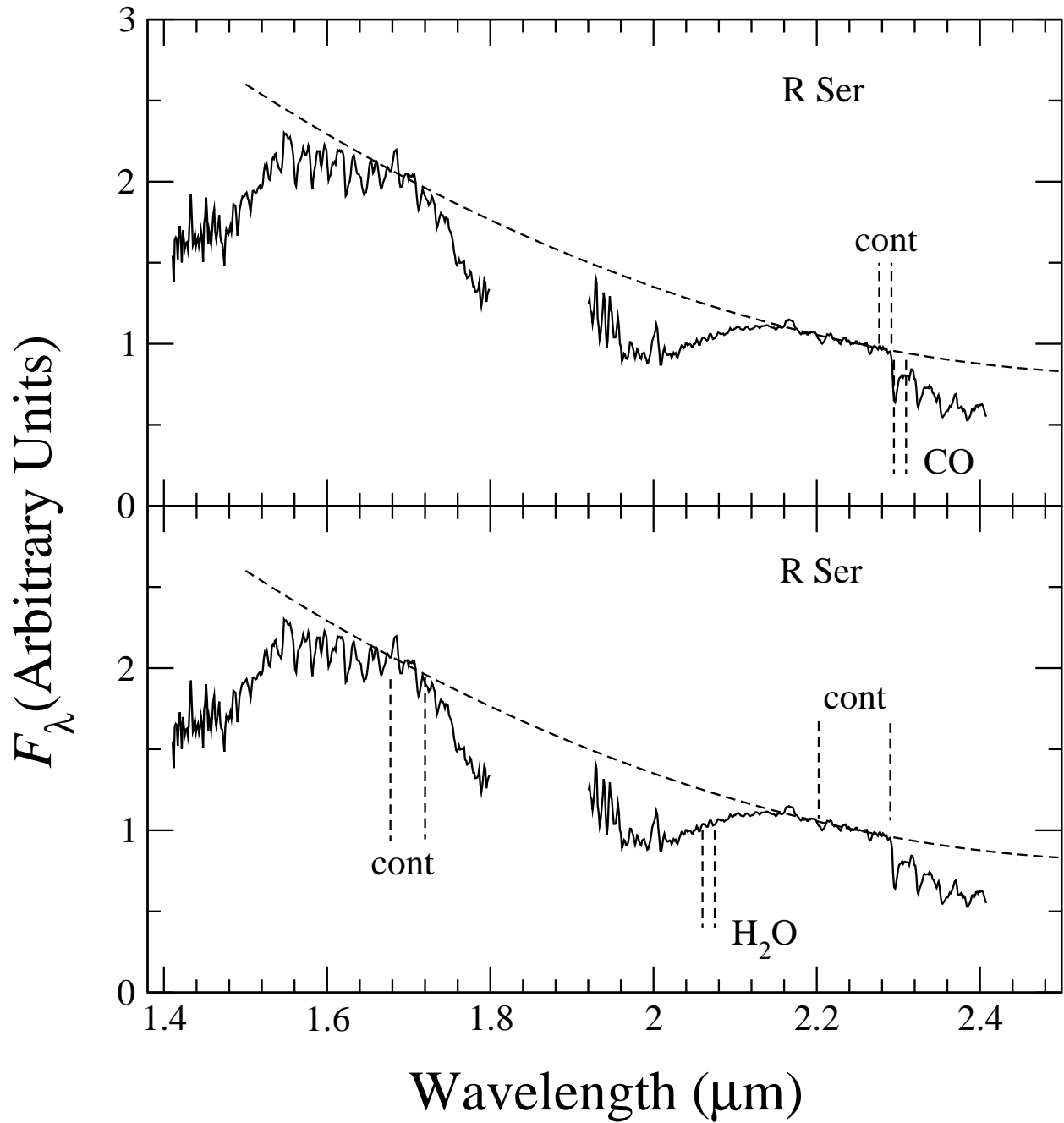


Fig. 1.— H and K spectra of the asymptotic giant branch (AGB) star R Ser (M7 III, Mira) used to demonstrate the CO and H₂O measurements for all spectra. The CO strength is determined by the ratio of flux in the band centered at 2.302 μm compared to the flux in the continuum band (in the star, not the fit) at 2.2875 μm (the bands are indicated with vertical *dashed* lines in the *upper* panel). The *dashed* curves are quadratic fits to the continuum in bands at 1.68–1.72 μm and 2.20–2.29 μm (as indicated in the *lower* panel). The H₂O strength is measured using the flux in a band at 2.060–2.075 μm relative to the flux in the fit at the same position (as indicated in the *lower* panel).

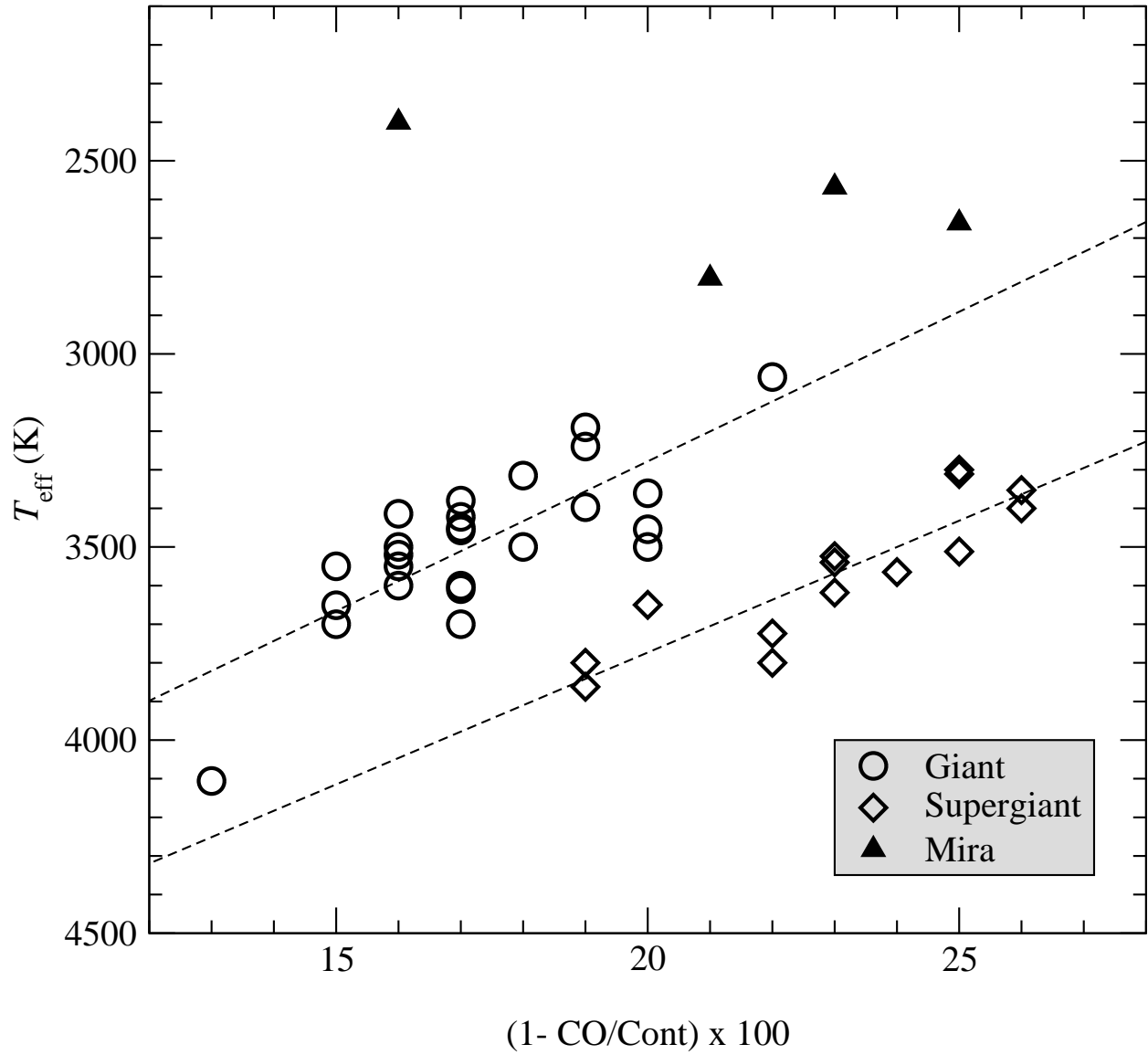


Fig. 2.— $2.3 \mu\text{m}$ CO absorption strength for the comparison stars. CO strength increases with decreasing T_{eff} but also with increasing luminosity; see text. The correlation appears to break down for some long period variables (Miras); see text.

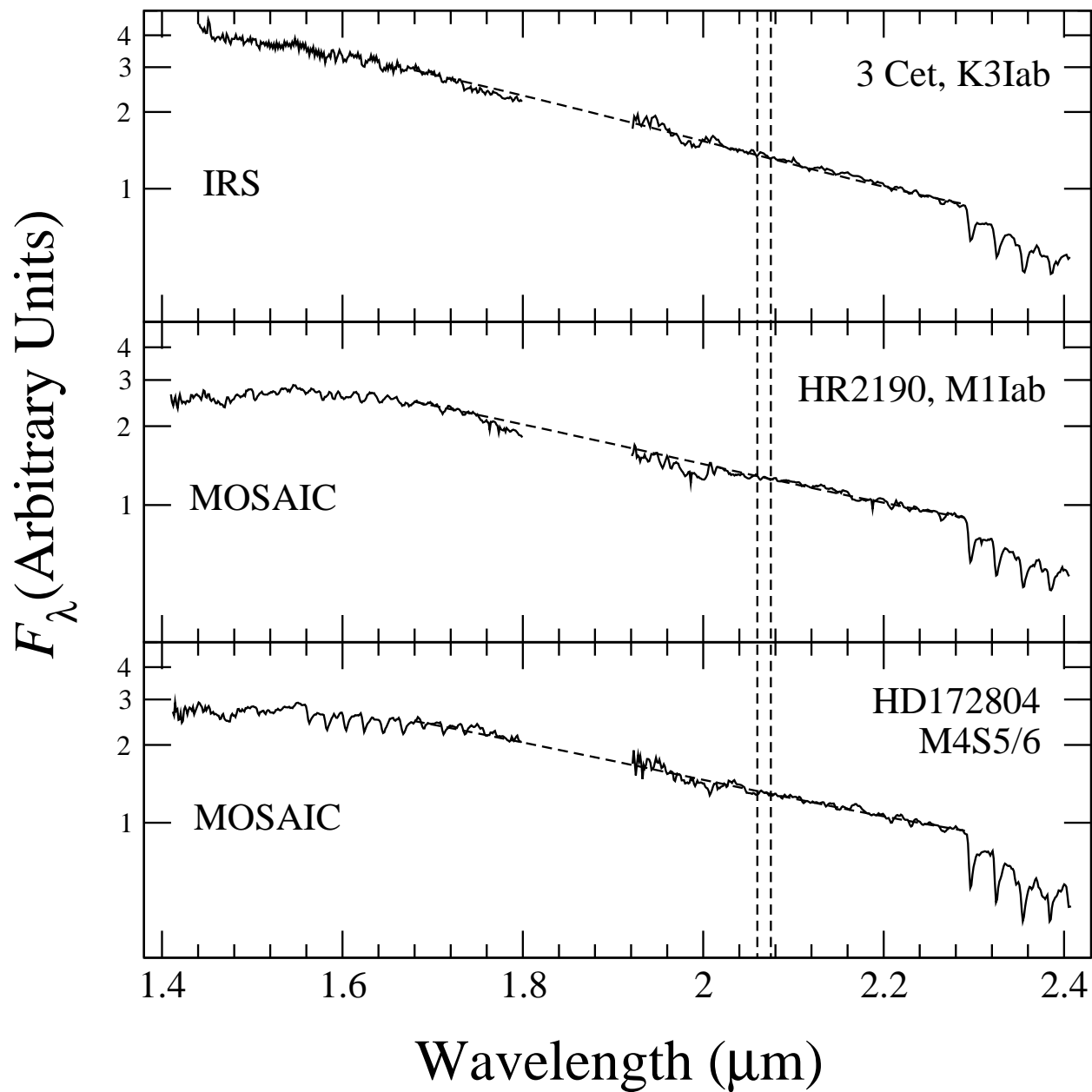


Fig. 3.— H and K spectra of late-type supergiants. Note the increase in CO ($2.3 \mu\text{m}$) absorption strength for later types. The *dashed* curves are the fits to the continua used to measure H_2O at the position of the vertical *dashed* lines (see text and Figure 1). Y axis scaled is logarithmically.

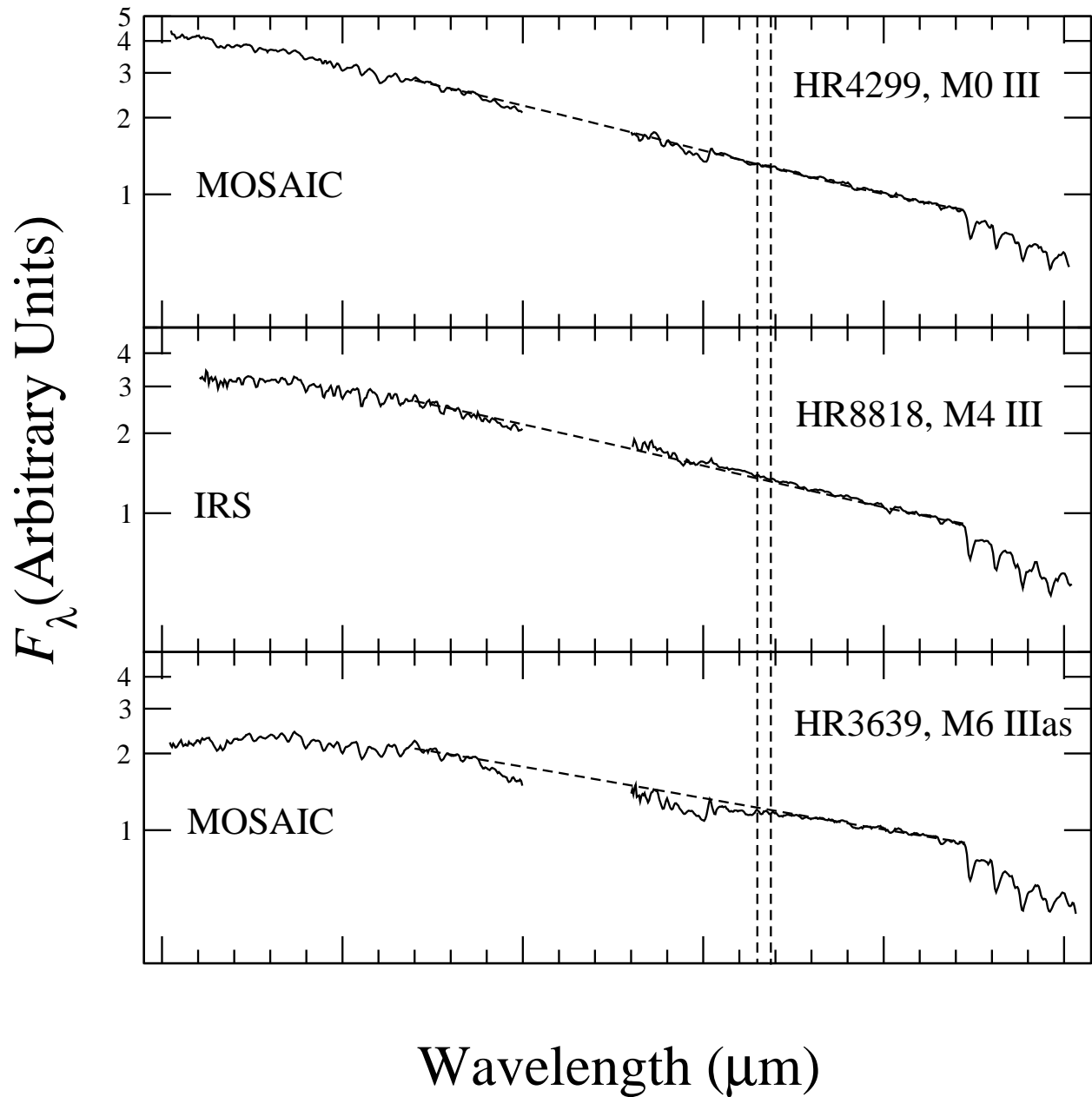


Fig. 4.— Same as Figure 3 but for late-type giants. HR3639 has similar CO strength compared to 3 Cet, but visibly stronger H_2O (Figure 3). Y axis is scaled logarithmically.

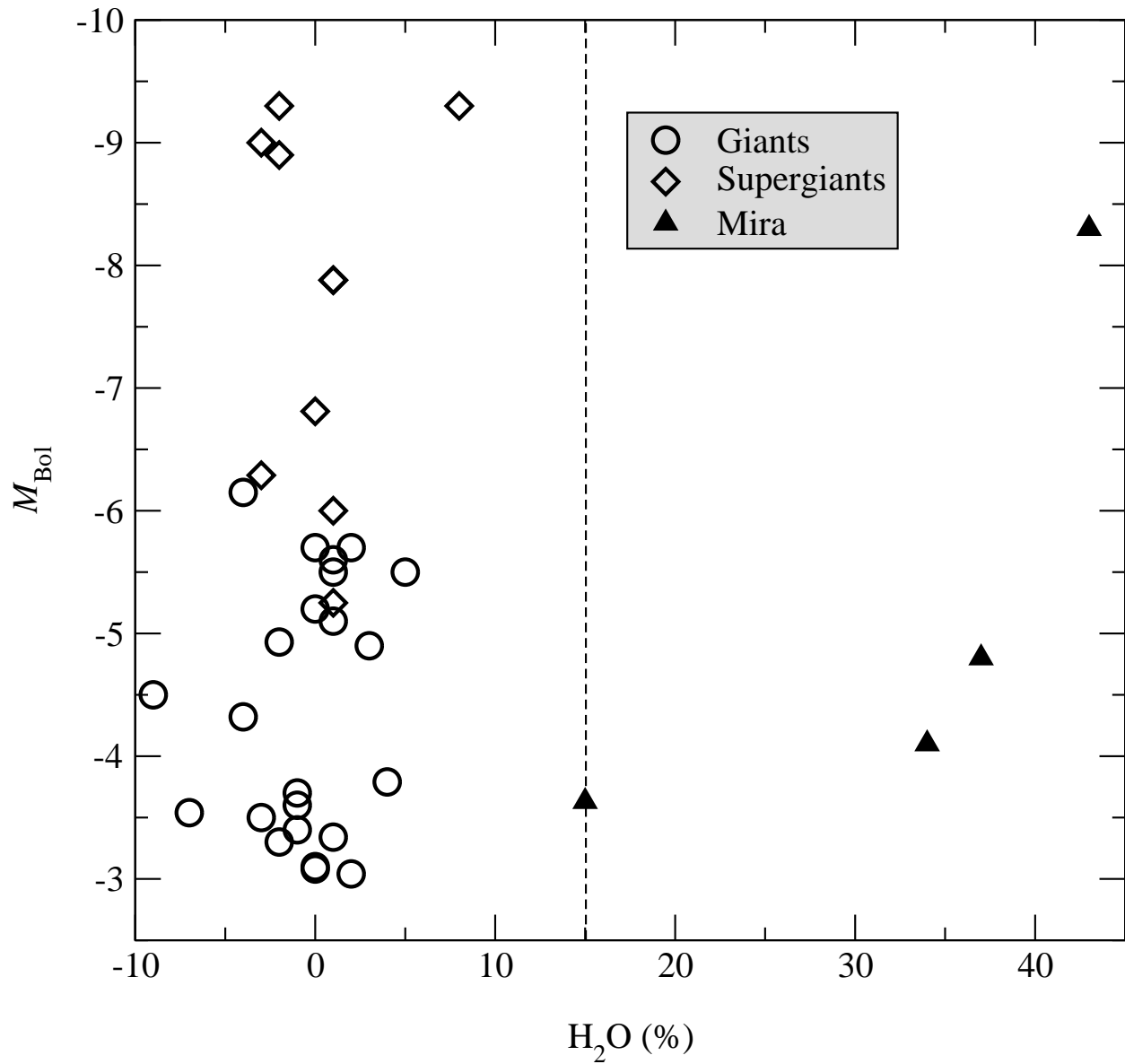


Fig. 5.— H_2O absorption strength for comparison stars. Stars with $\text{H}_2\text{O} \geq 15\%$ are known Miras (long period variables, or LPVs). All Galactic center stars with H_2O greater than 15% were classified as LPV candidates with a correspondingly lower T_{eff} ; see text.

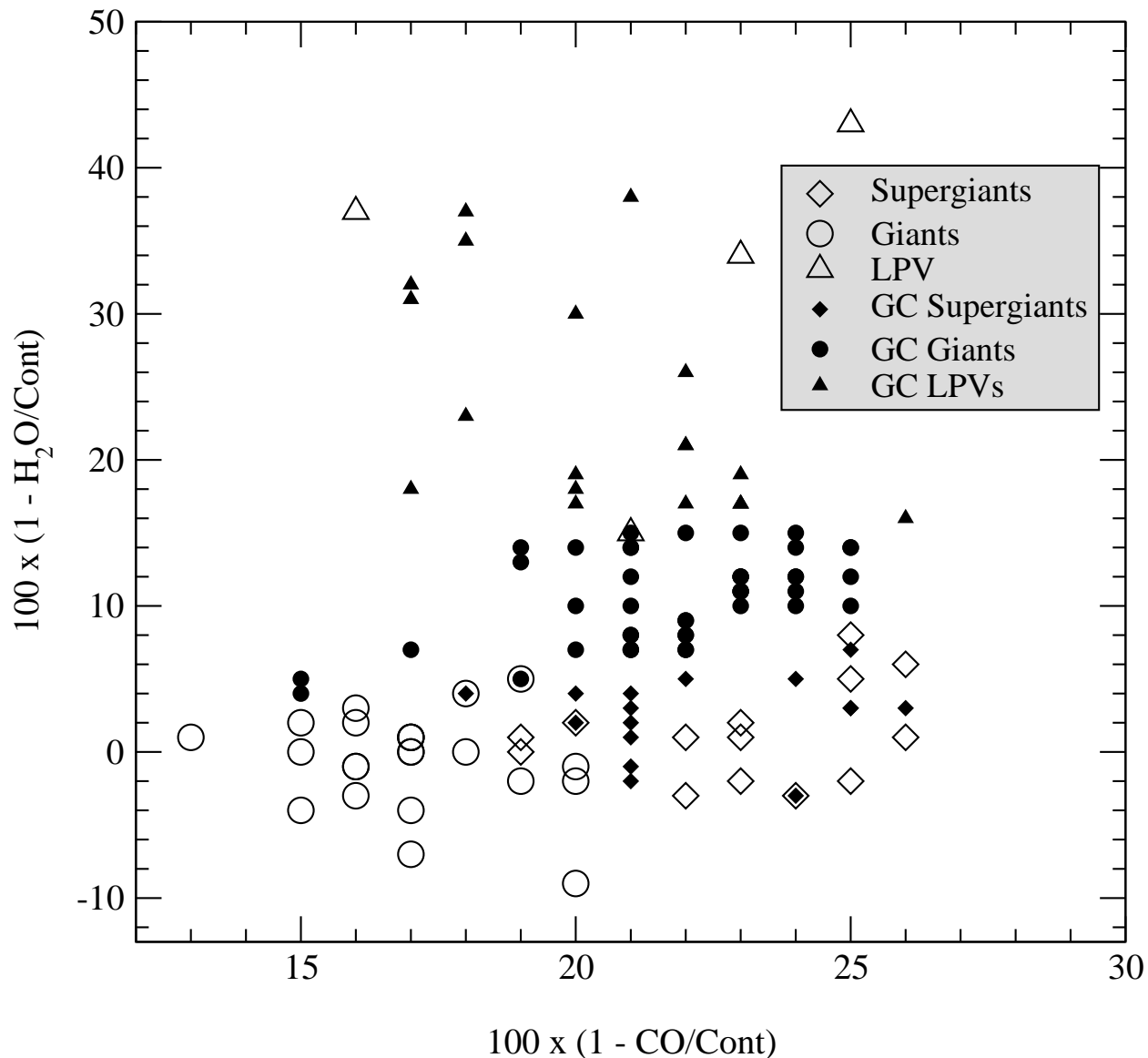


Fig. 6.— H₂O strength vs CO strength for the Galactic Center (GC) and comparison stars. The comparison stars are shown as *open* symbols while GC stars are plotted with *filled* symbols. For a given CO strength, GC stars classified as III have larger H₂O than those classified as I. The GC III stars lie between the warmer comparison stars and cooler comparison star LPVs. GC stars with H₂O > 15 % are classified as LPVs or LPV candidates (LPV? in Table 6).

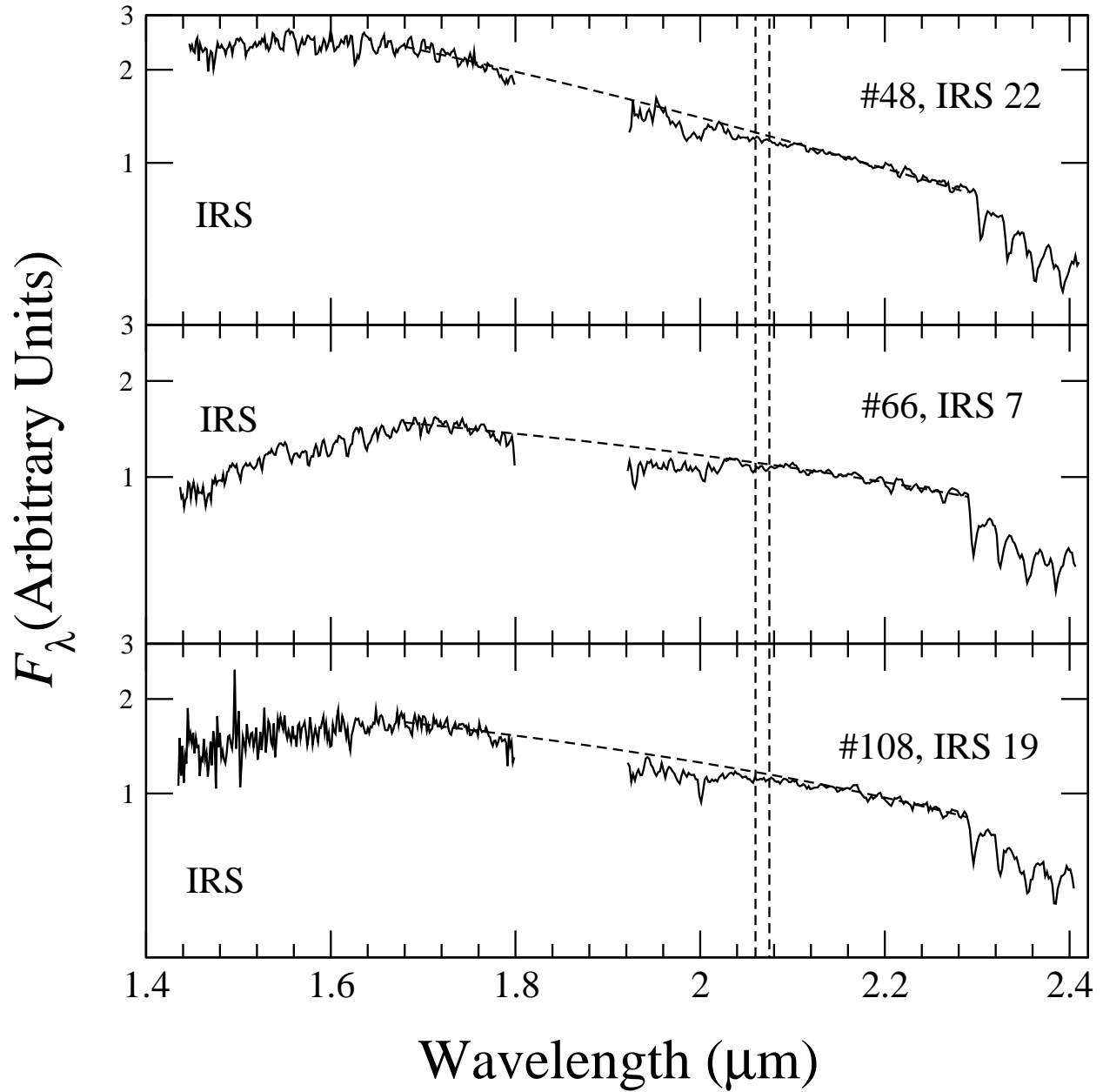


Fig. 7.— Example spectra of stars classified as supergiants in the Galactic center. These stars were analyzed at high spectral resolution by Ramírez et al. (2000) and Carr et al. (2000). The *dashed* curves are the fits to the continua used to measure H_2O at the position of the vertical *dashed* lines (see text and Figure 1). Y axis is scaled logarithmically.

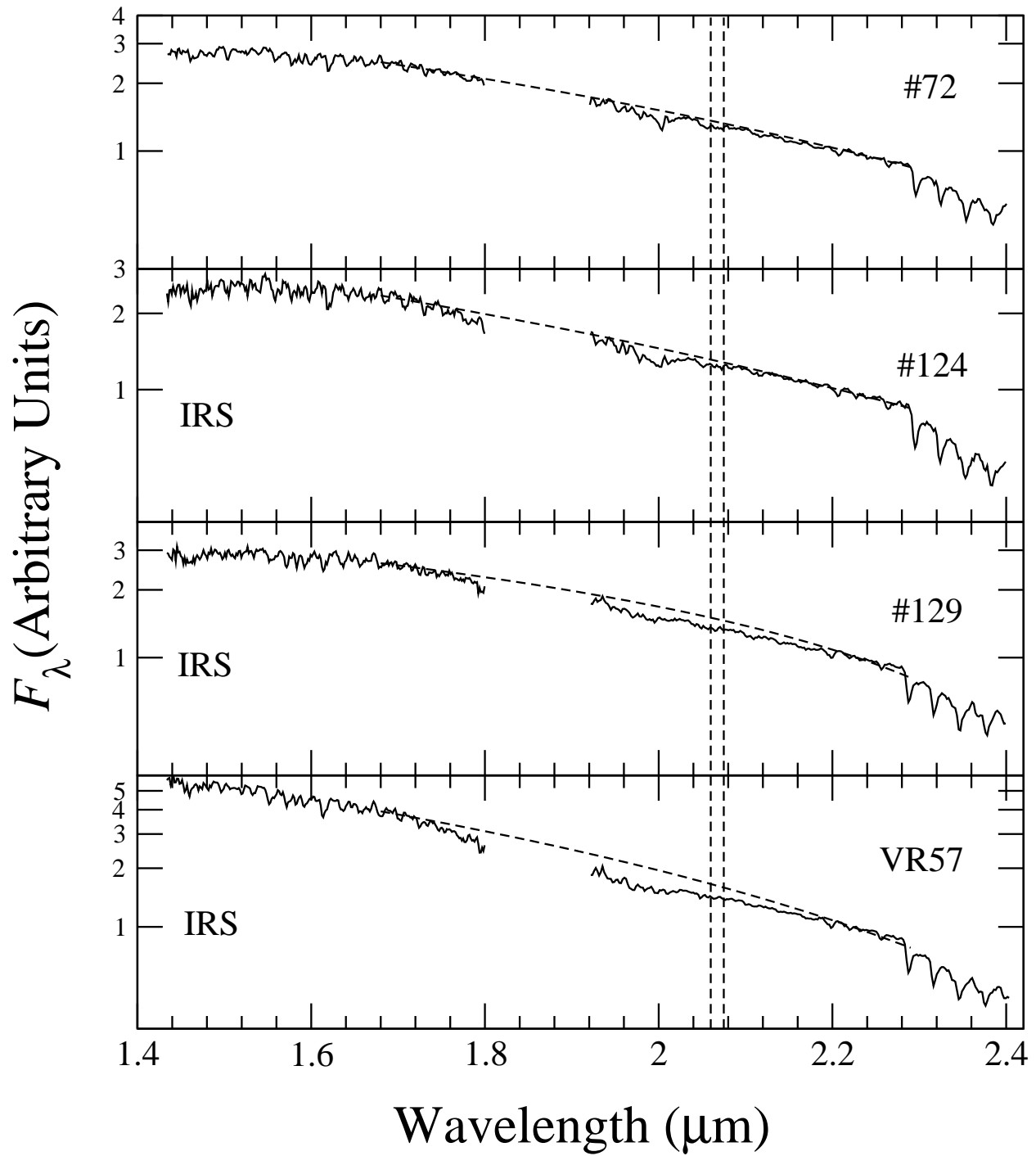


Fig. 8.— Same as Figure 7. Star 72 is classified as a giant; all others are supergiants. These stars were analyzed at high spectral resolution by Ramírez et al. (2000).

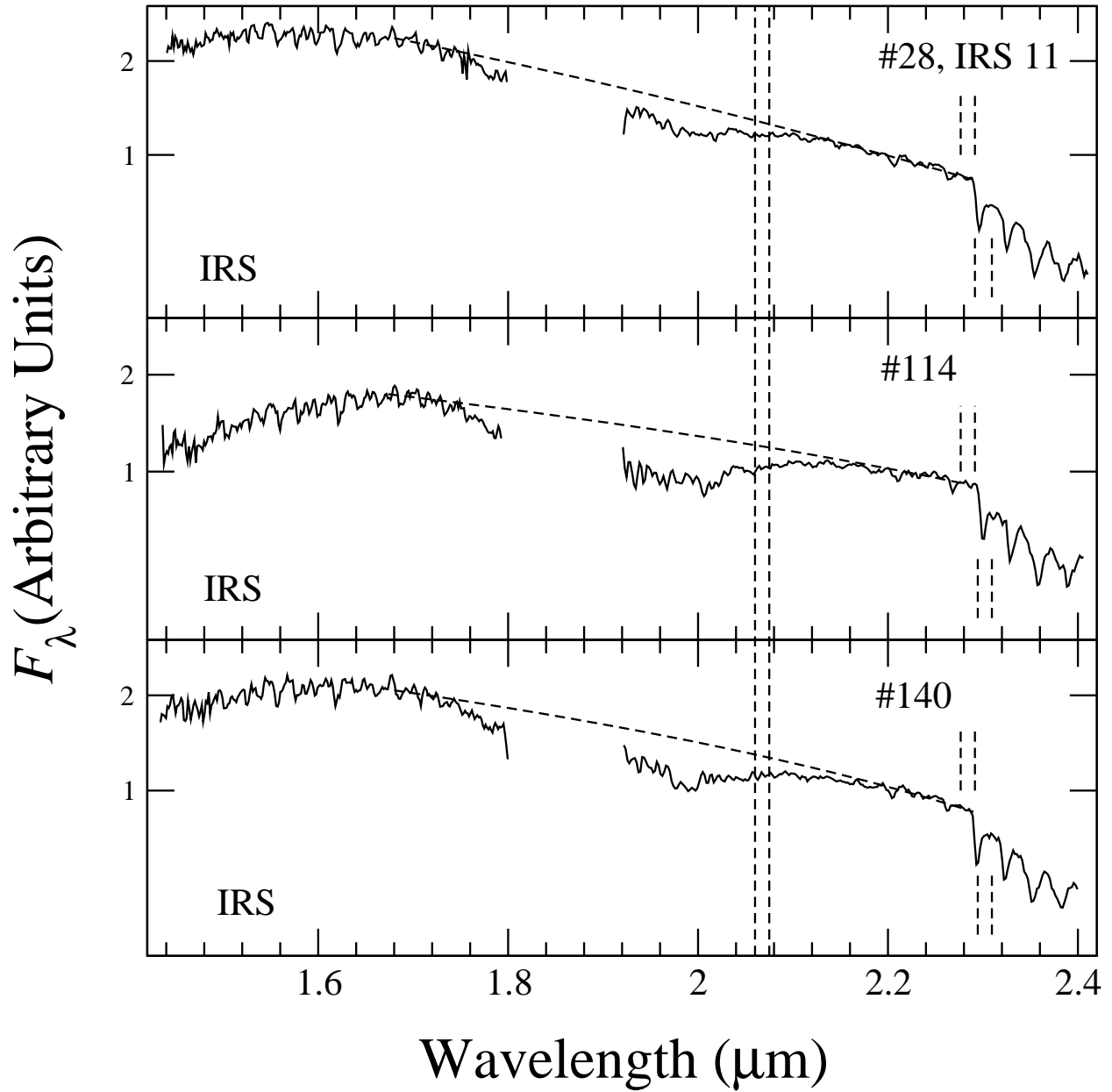


Fig. 9.— Example spectra of stars classified as asymptotic giant branch (referred to in the text as AGB, giant, or III stars) stars in the Galactic center. Stars #28, #114, and #140 were analyzed at high spectral resolution by Ramírez et al. (2000). The *dashed* curves are the fits to the continua used to measure H_2O at the position of the vertical *dashed* lines (see text and Figure 1). Y axis is scaled logarithmically.

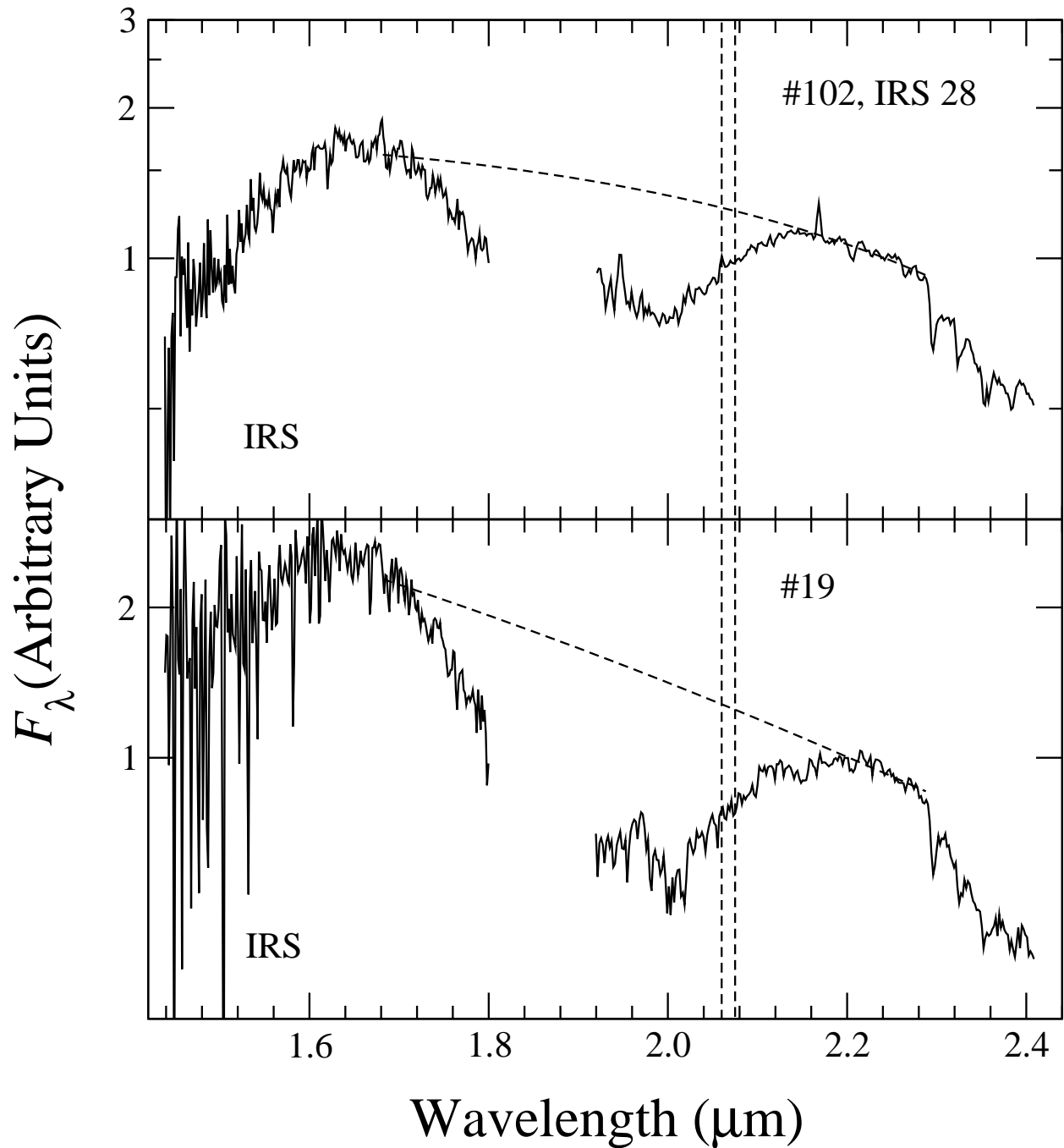


Fig. 10.— Stars classified as long period variables (LPV) or candidate LPVs (LPV? in Table 6) in the Galactic center. IRS 28 is a known photometric variable; see text. The emission-line near $2.17 \mu\text{m}$ evident in the spectrum of IRS 28 is likely due to incomplete subtraction of the local nebular background. The *dashed* curves are the fits to the continua used to measure H_2O at the position of the vertical *dashed* lines (see text and Figure 1). Y axis is scaled logarithmically.

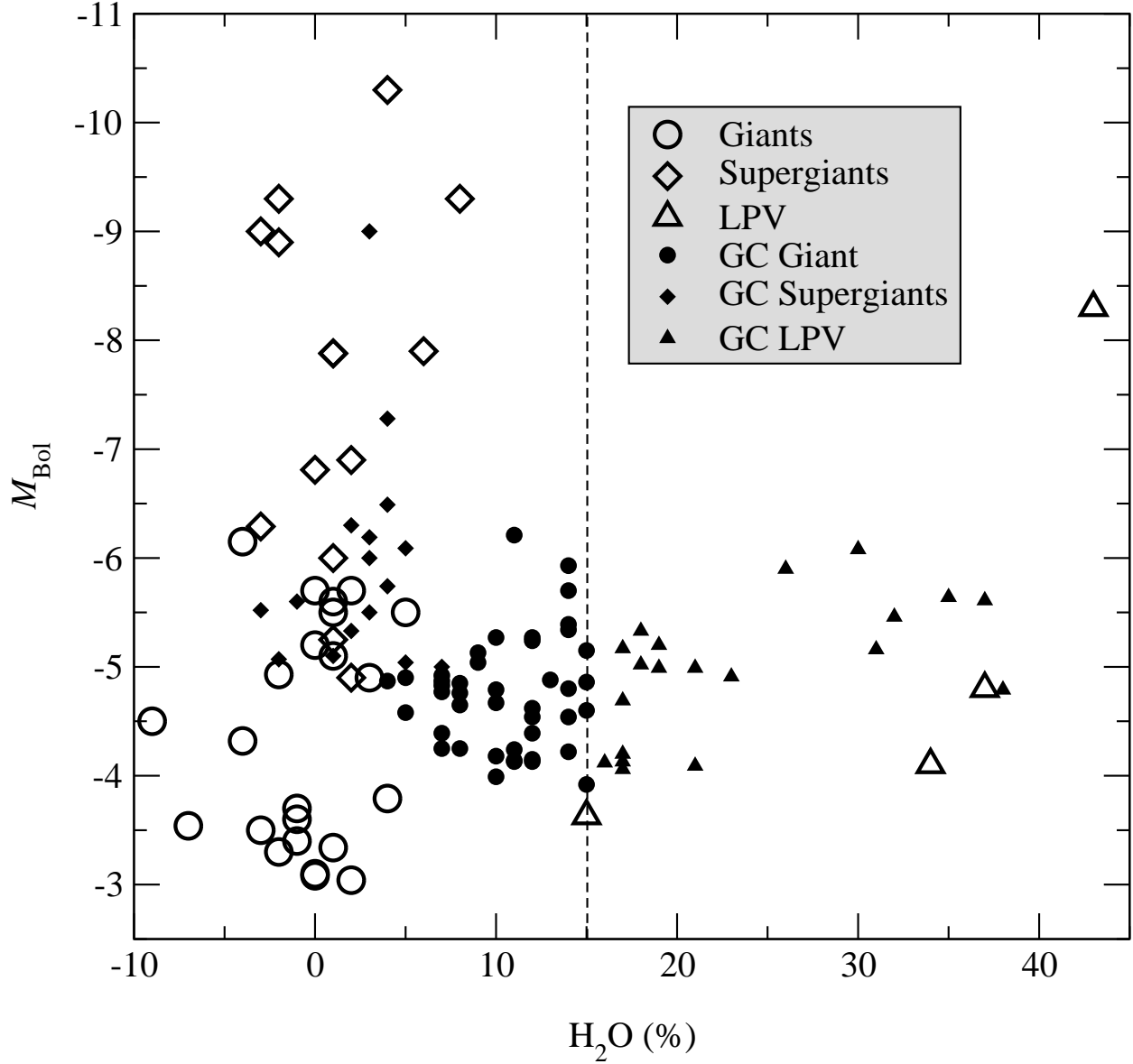


Fig. 11.— Comparison and Galactic Center (GC) star M_{bol} vs. H_2O strength plot. The comparison stars are shown as *open* symbols while GC stars are plotted with *filled* symbols. The assigned GC luminosity classes are consistent with the comparison star luminosity ranges. The plot shows we have observed later type giants in the GC than are represented in the warmer comparison III sample, and these GC IIIs lie between the comparison IIIs and LPVs, not along the comparison I track which runs vertically in this diagram (see text for details, and also Figure 6).

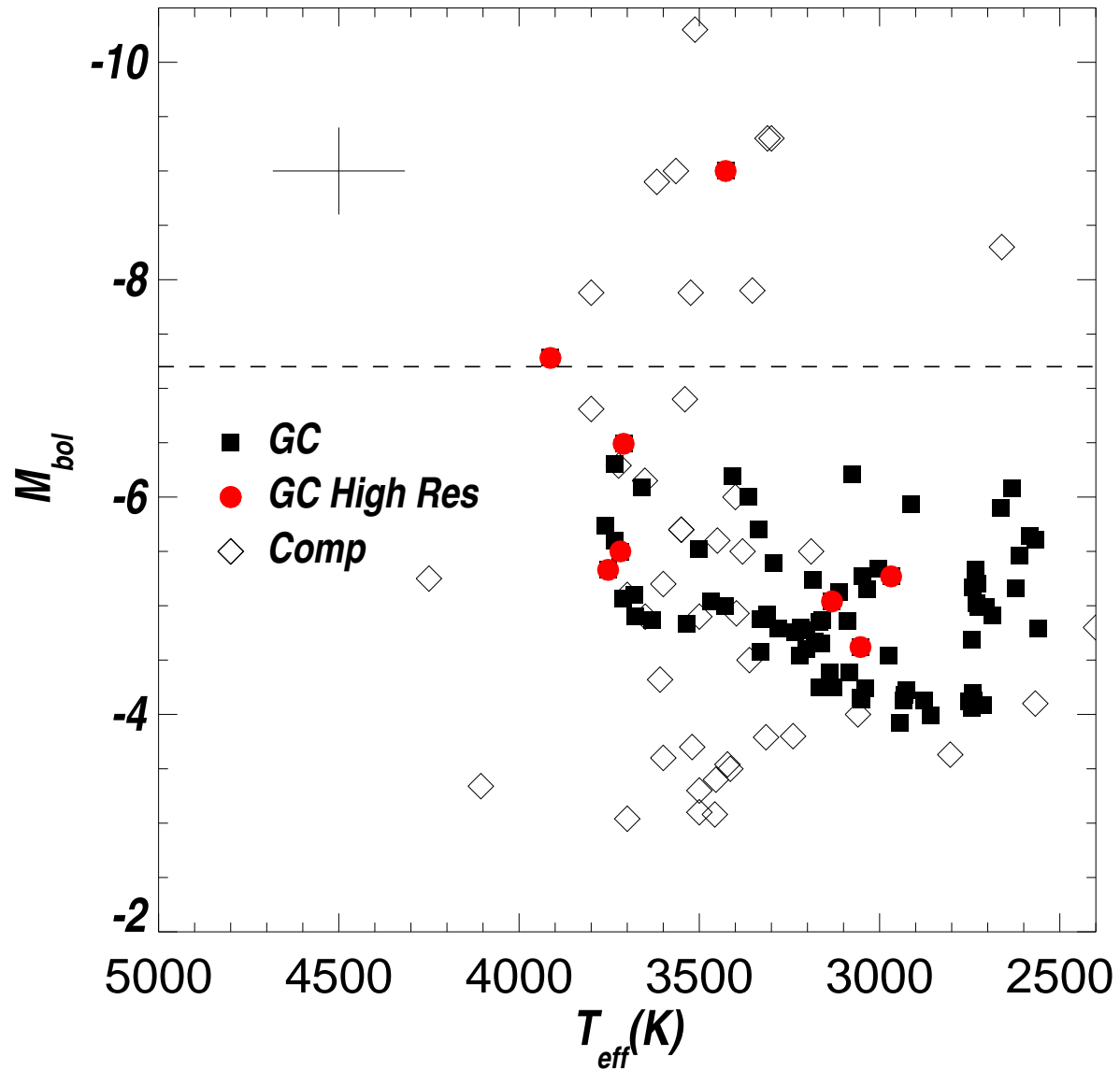


Fig. 12.— Hertzsprung–Russell diagram for the Galactic center (GC) stars (shown as *closed* squares with typical uncertainty given by the error bar in the upper left corner) and comparison stars (Comp, plotted as *open* diamonds). The GC stars analyzed at high spectral resolution by Carr et al. (2000) and Ramírez et al. (2000) are plotted as *filled* circles.

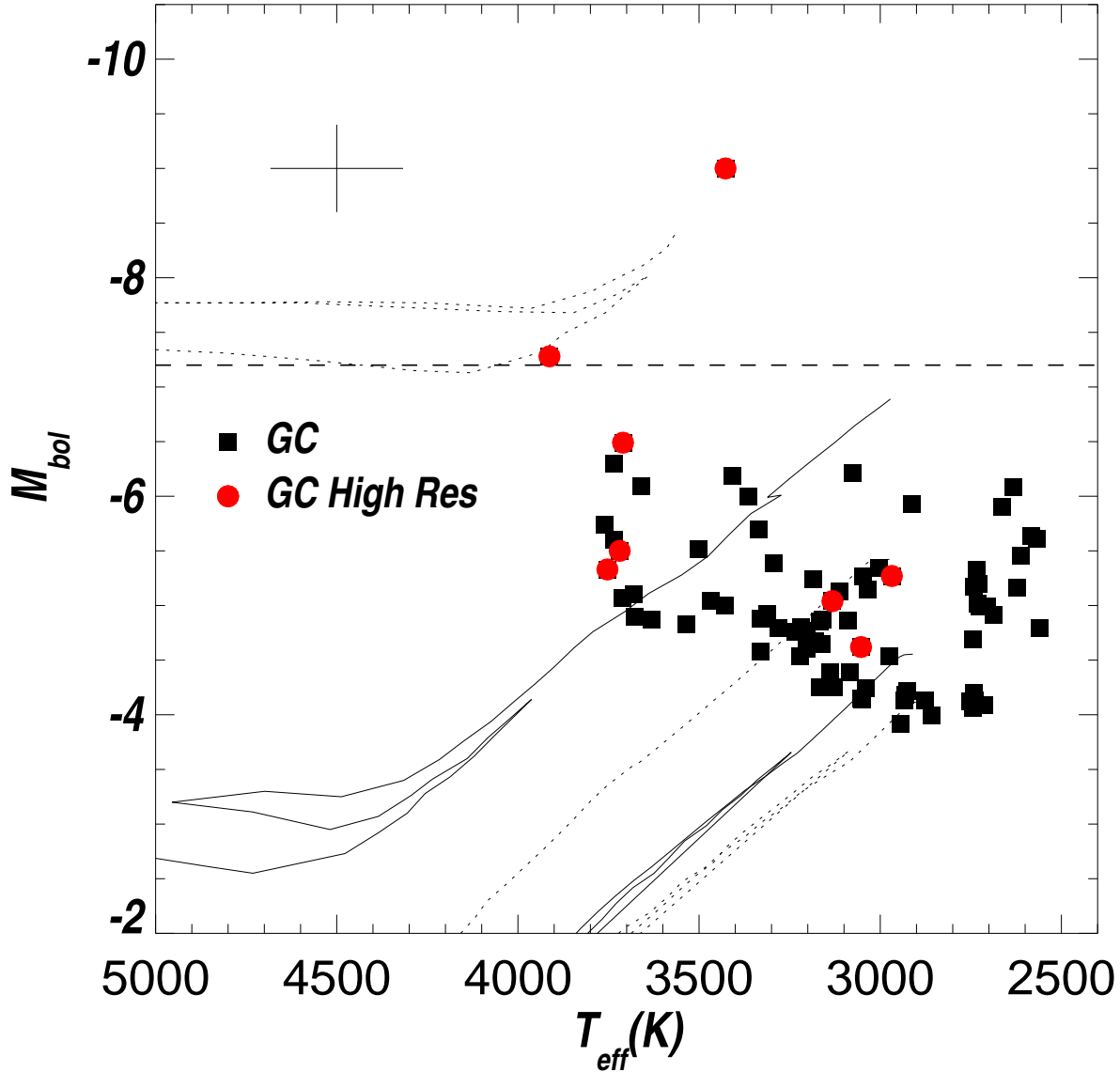


Fig. 13.— Galactic center (GC) stars plotted as in Figure 12, but with $[Fe/H] = 0.0$ isochrones plotted as well. The isochrones are from Bertelli et al. (1994) for age < 100 Myr and Girardi et al. (2000) otherwise. Isochrones are plotted for ages of 10 Myr, 100 Myr, 1 Gyr, 5 Gyr, and 12 Gyr. The models have $[Fe/H] = 0.0$ for all ages, and these appear to better represent the data than models with lower metallicity at older ages ($[Fe/H] = -0.2$); see Figure 12c and text. Neither set of isochrones reaches the coolest stars (long period variable candidates with $T_{eff} < 2800$ K), but the $[Fe/H] = 0.0$ isochrones extend to cooler temperatures and thus fit more Galactic stars than the $[Fe/H] = -0.2$ isochrones. Comparison to the isochrones shows that all the GC stars classified as giants (Table 6, III) are AGB stars; they are too luminous to be first ascent giants. This is a consequence of the selection criteria. The horizontal line segment at $M_{bol} = -7.2$ in each panel indicates the approximate observed luminosity above which only supergiants lie (Blum et al. 1996b).

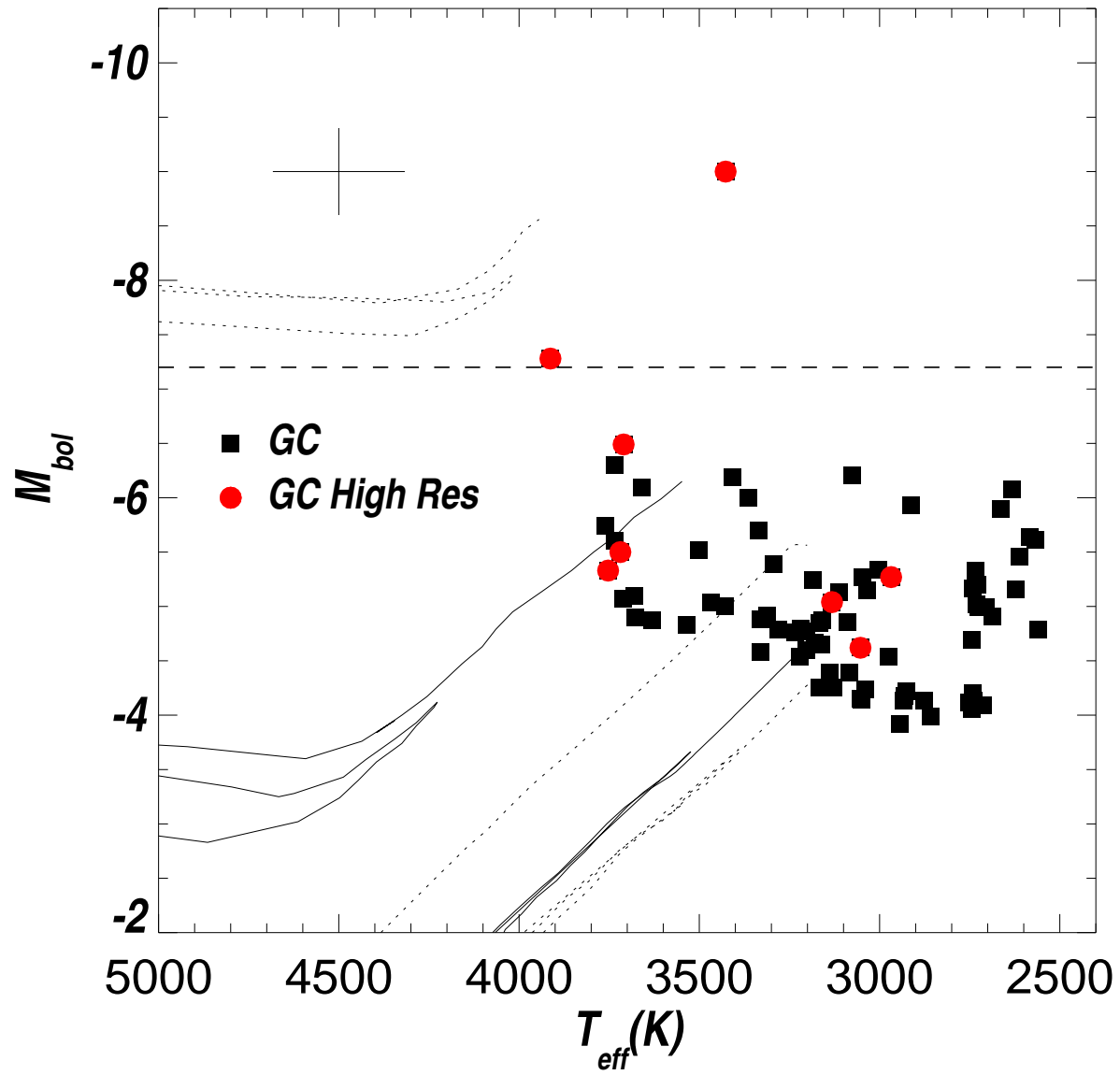


Fig. 14.— Same as for Figure 12b, but with $[Fe/H] = -0.2$ isochrones plotted.

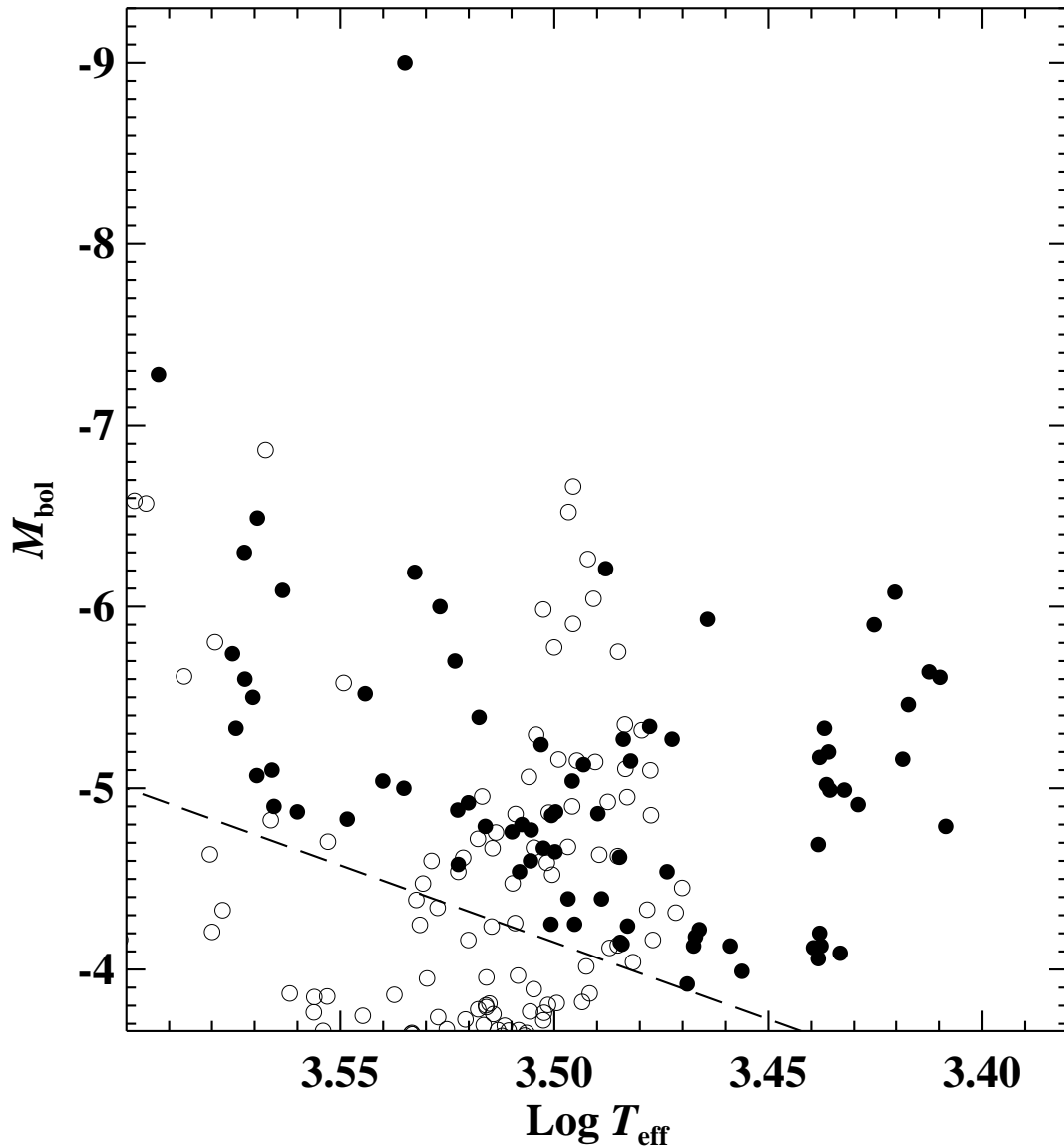


Fig. 15.— Hertzsprung–Russell diagram for the Galactic Center (GC) stars (*filled circles*) compared to a model with constant star formation rate (*open circles*). This figure demonstrates that the models cover the same parameter space as the GC data, including the pronounced intermediate age feature at $T_{\text{eff}} \approx 3200$ K ($\log_{10}(T_{\text{eff}}) = 3.50$), $M_{\text{bol}} \approx -5.0$, except for the coolest GC stars ($\log_{10}(T_{\text{eff}}) > 3.45$); see text. The model points include objects below our observed magnitude cut-off (the region below the *dashed* line).

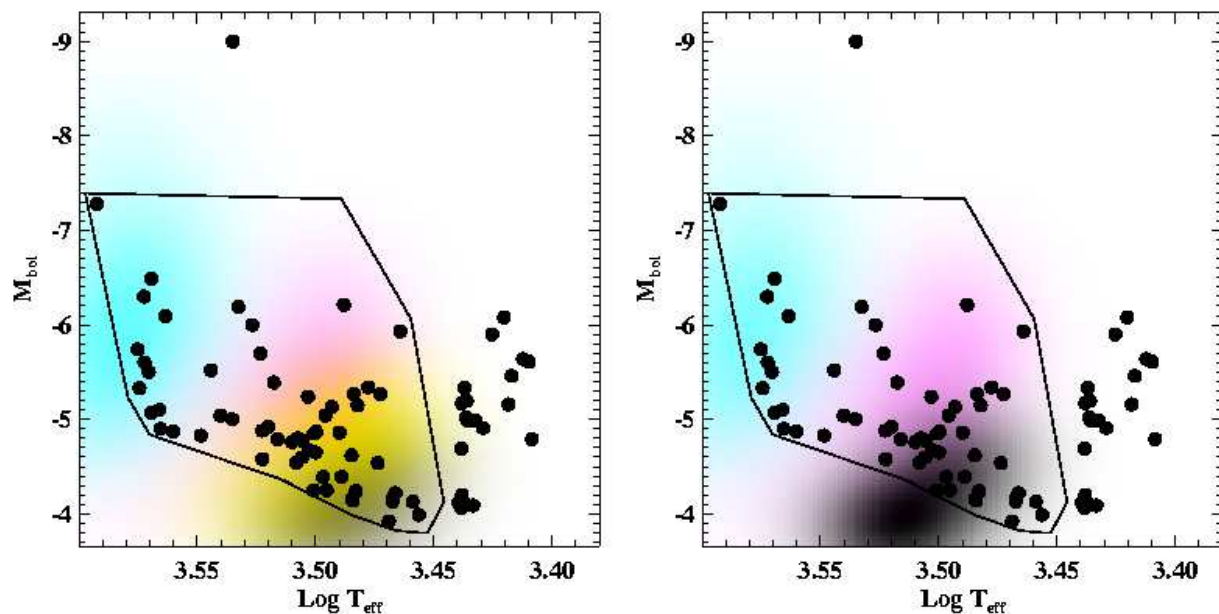


Fig. 16.— Comparison of the best fitting star formation history with solar metallicity throughout (*left* panel, Model A, Table 7) and with $[\text{Fe}/\text{H}]=-0.2$ for ages ≥ 5 Gyr (*right* panel, Model B, Table 7). Darker regions represent higher number density. *Cyan* corresponds to ages between 10 and 100 Myr, *magenta* 100 Myr to 1 Gyr, *yellow* 1 Gyr to 5 Gyr, and *gray* to 5 Gyr to 12 Gyr. The purely solar metallicity model fits the data better; see text. Model B (*right* panel) has a best fit solution with no SF in the 3rd (1–5 Gyr) bin (this is why no *yellow* region appears; see Figure 18). However, a low metallicity ($[\text{Fe}/\text{H}] \lesssim -0.6$), very old (> 12 Gyr) component would not be detected by our sample. The dark polygons in each panel represent the area of the model and observational parameter space used in the fits. The coolest stars are not accounted for by the models, and so were not used in the fits (i.e. those stars outside the polygon), neither was the brightest star, IRS7 (Age < 10 Myr).

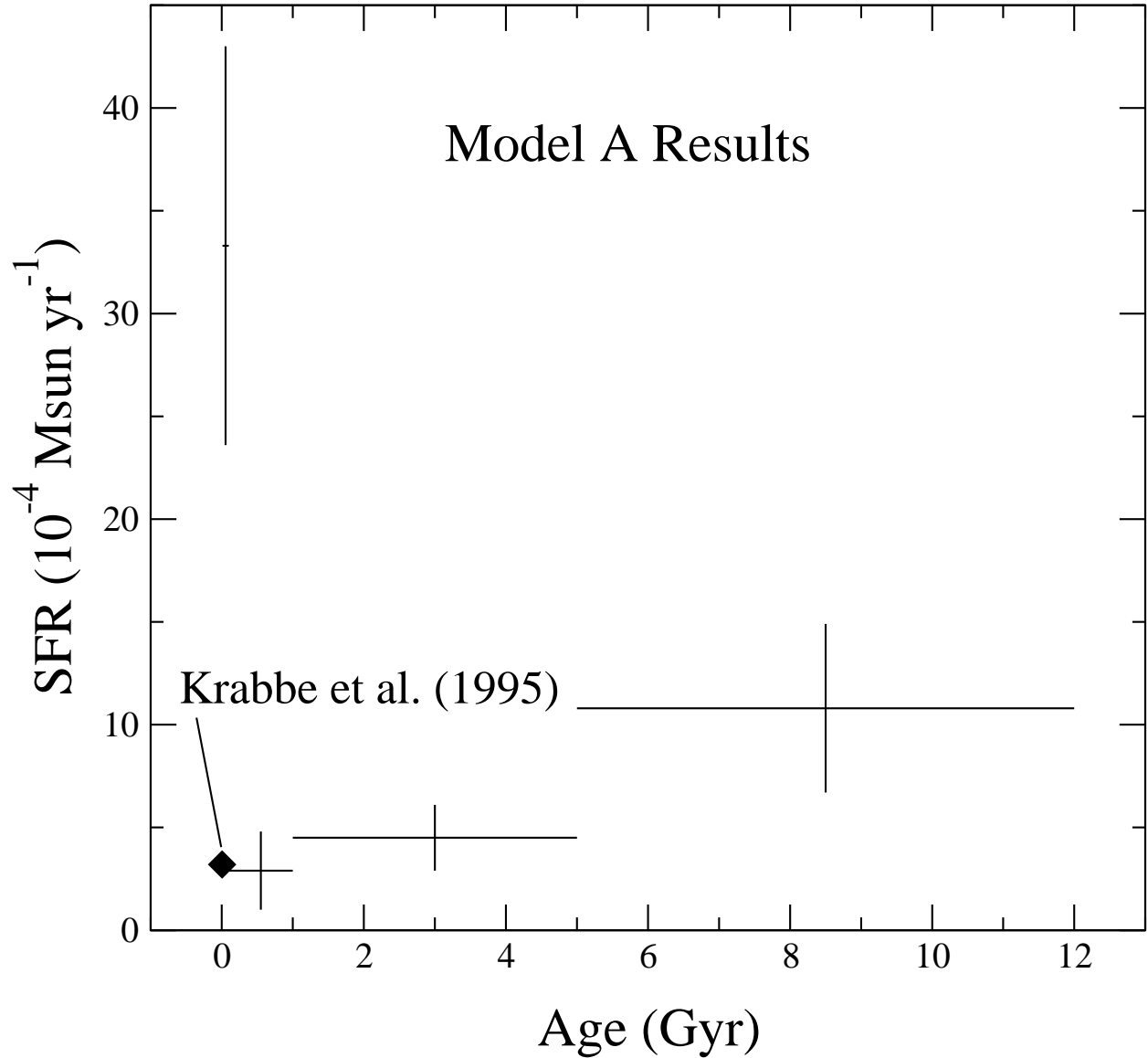


Fig. 17.— Star formation history (SFH) for the Galactic center (see Table 7). The crosses represent the results to the SFH fits to the Hertzsprung–Russell Diagram (Figure 13) for Model A with solar $[\text{Fe}/\text{H}]$ through out. Model A provides the best fit; see text. The age bins correspond to the horizontal width of the crosses and are 10 Myr – 100 Myr, 100 Myr – 1 Gyr, 1 Gyr – 5 Gyr, and 5 Gyr – 12 Gyr. The vertical height of each cross is the one sigma error in the star formation rate for the respective bin. The *filled* diamond represents the star burst model from Krabbe et al. (1995) averaged over 10 Myr and is placed at 5 Myr along the age axis (i.e., it is the youngest point in the plot).

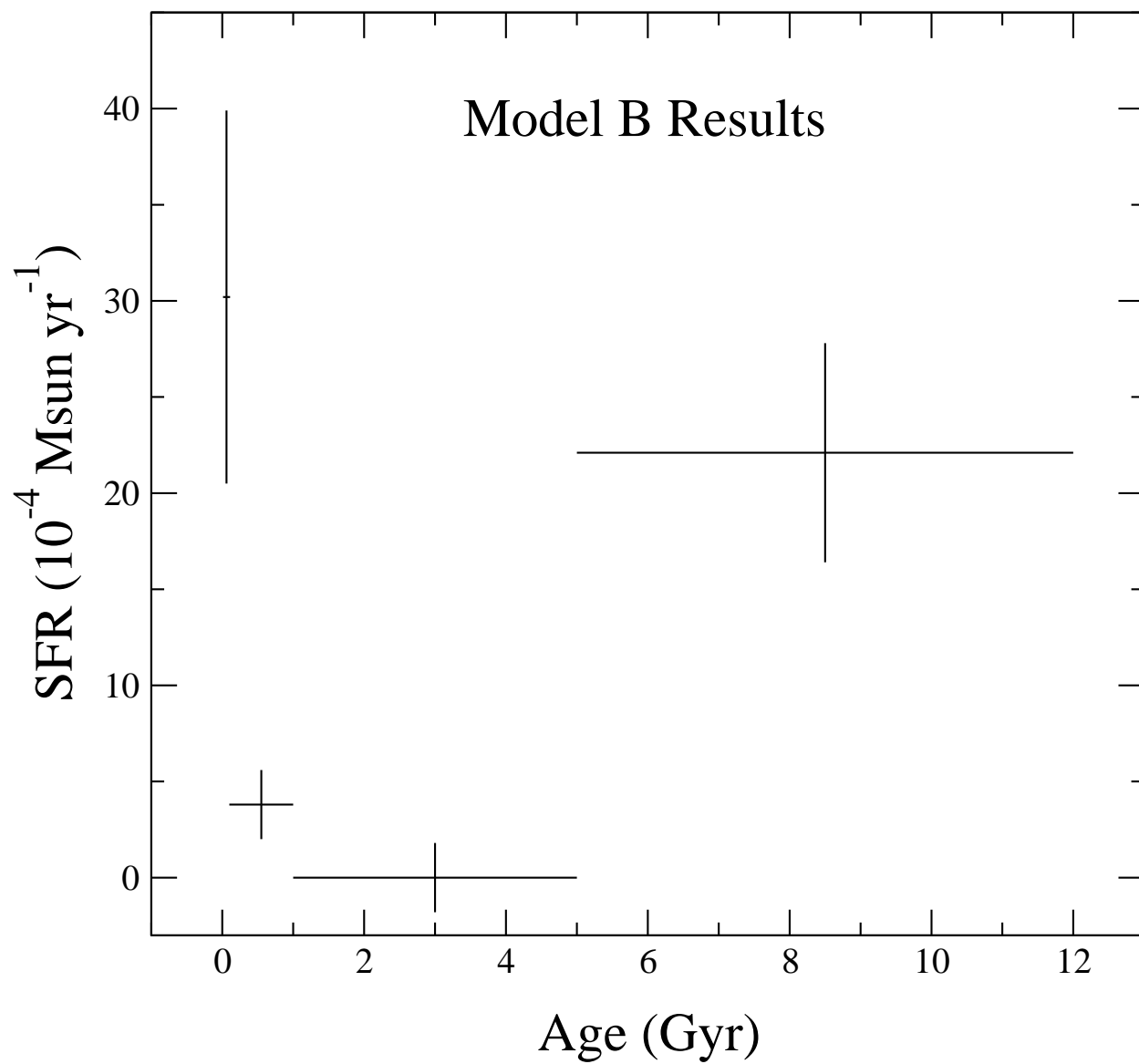


Fig. 18.— Same as Figure 17, but for Model B with $[\text{Fe}/\text{H}] = -0.2$ in the oldest age bins. Model A (Figure 15a) provides a better fit; see text.

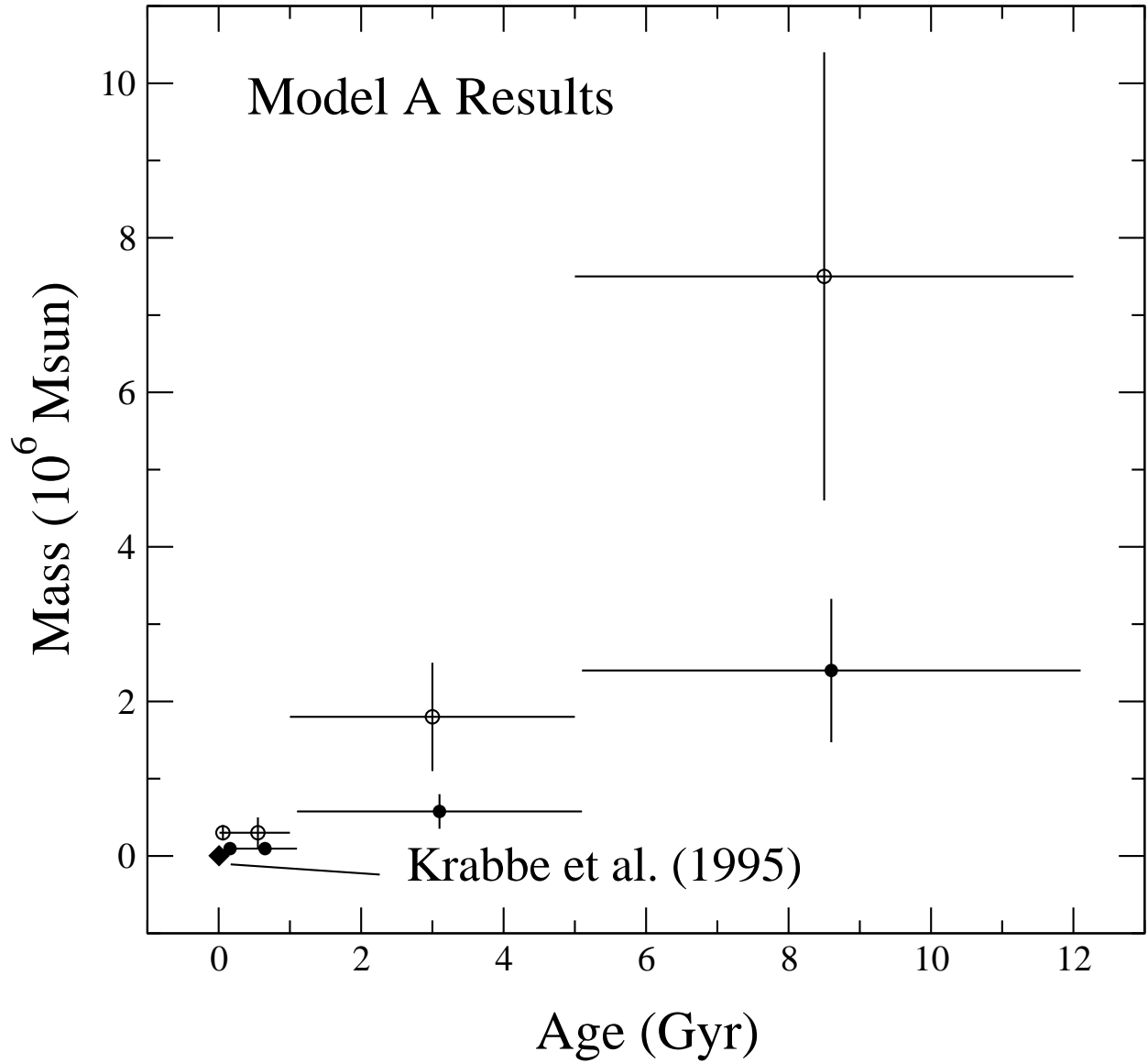


Fig. 19.— Total mass (*open circles*) in stars formed in each corresponding age bin (10 Myr – 100 Myr, 100 Myr – 1 Gyr, 1 Gyr – 5 Gyr, and 5 Gyr – 12 Gyr) for Model A of Figure 17; see also Table 7. The Krabbe et al. (1995) result for a ~ 5 Myr old burst which produces $3200 M_{\odot}$ is shown. The *filled circles* represent the present day mass for the same star formation history accounting for the mass loss due to stellar winds. The total present day mass is consistent with the dynamical mass determinations; see text. The *filled circles* have been shifted by 0.1 Gyr in the Figure for clarity.

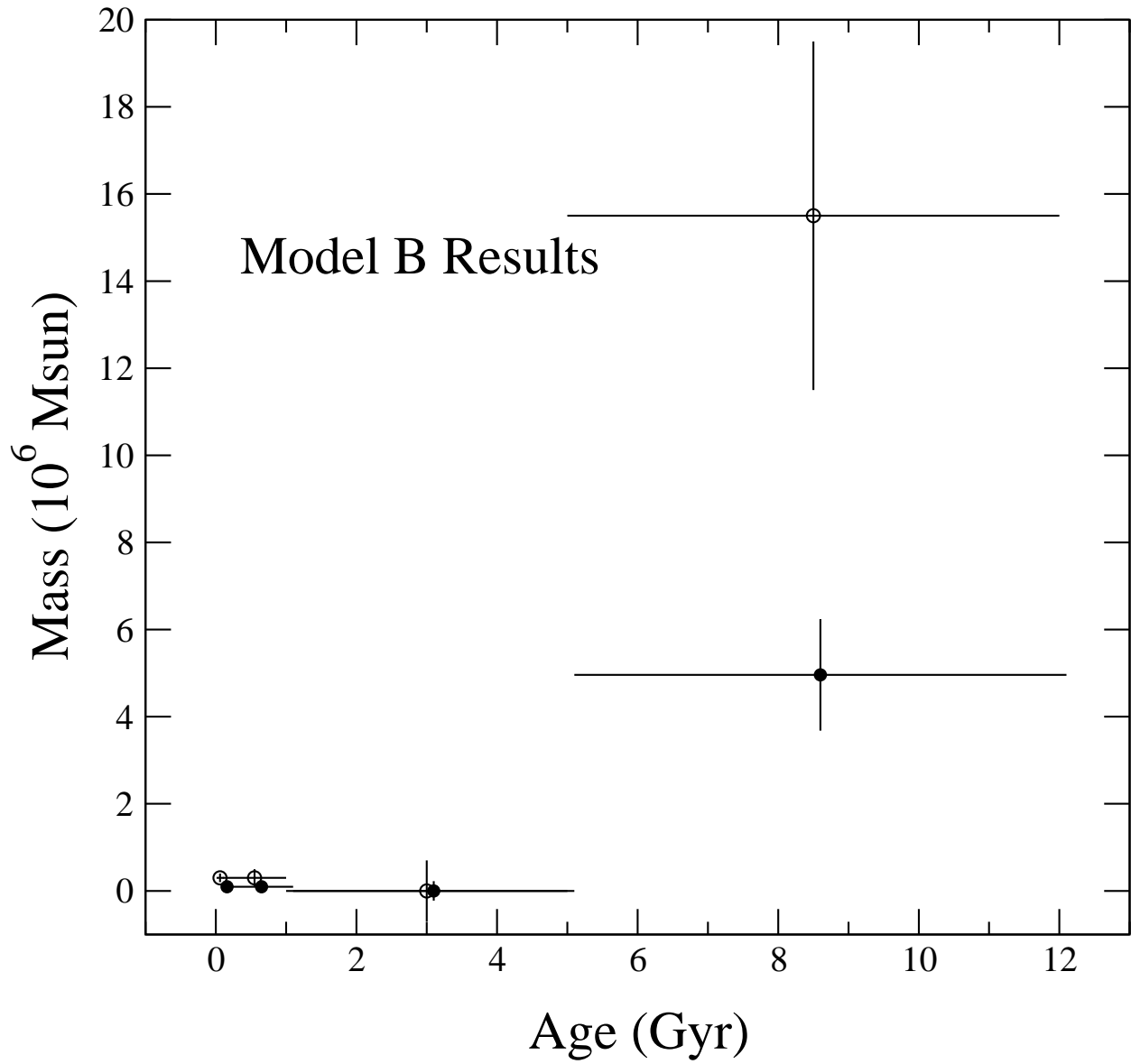


Fig. 20.— Same as Figure 19, but for Model B results.